OPTICAL WAVEGUIDES AND INTEGRATED TRIPLEXER FILTER

OPTICAL WAVEGUIDES AND INTEGRATED TRIPLEXER FILTER

By

LEI ZHAO, B. SC.

A Thesis

Submitted to the School of Graduate Studies

in Partial Fulfilment of the Requirements

for the Degree

Master of Applied Science

McMaster University

MASTER OF APPLIED SCIENCE (2007) McMaster University

Electrical and Computer Engineering Hamilton, Ontario

TITLE: Optical waveguides and integrated triplexer filter

AUTHOR: Lei Zhao, B.SC. (McMaster University)

SUPERVISOR: Professor W.P. Huang

NUMBER OF PAGES: xi, 66

Abstract

The modeling, design and simulation of optical waveguides and integrated optical triplexer filters are presented. The work includes two subjects. One is application of improved three-point fourth-order finite-difference method and the other is design of triplexer optical filter for fiber-to-the-home passive optical network.

The improved three-point fourth-order finite-difference method utilizes special format of one dimensional Helmholtz Equation and adopts generalized Douglas scheme and boundary conditions matching at interface. The modal analysis of dielectric slab waveguides and metal slab waveguides that support Surface Plasmon Plaritons by using this improved fourth-order finite-difference method is compared by using traditional first-order central difference method. The application of using improved three-point fourth-order finite-difference method in modal analysis of optical fiber waveguide is also provided.

The modeling, design and simulation of monolithically integrated triplexer optical filter based on silicon wire waveguide are presented in detail. The design of this device facilitates multi-mode interference device (MMI) and arrayed waveguide grating (AWG) device to function as coarse wavelength division multiplexing and dense wavelength division multiplexing respectively. The MMI is used to separate downstream signs for upstream signal and AWG is used to further separate two down-stream signals with different bandwidths required. This design is validated by simulation that shows excellent performance in terms of spectral response as well as insertion loss.

Acknowledgement

I would like to express my deepest gratitude to my supervisor Dr. Wei-Ping Huang for his guidance and support.

I would also like to thank Dr. Chenglin Xu for his support on triplexer optical filter design and assistance on using Apollo's APSS software.

I wish to express my appreciation to those who helped during my research. This includes Dr. Changqing Xu, Dr. Xu Li , Dr. Li Yang, Dr. Xiaobin Hong, Dr. Dong Zhou and Qingyang Xu.

My deepest appreciation belongs to my wife and my parents for their constant love and support to keep me energetic.

Index of contents

List of figures

List of tables

Chapter 1

Introduction

1.1 Background

The finite-difference (FD) method is an important technique in both mode solver and beam propagation method (BPM) in terms of accuracy and efficiency. The formulas of FD greatly affect accuracy and efficiency of the finite-difference methods. Stern [1] derived semi-vectorial formula in which interface condition was averaged by refractive indexes on both sides, and it is considered as the conventional FD formula with first order accuracy. Vassallo [2] derived a formula from Taylor Expansion and matching boundary conditions for step-index waveguide. However, this formula is second-order accurate if interface is in the middle of grid points, which is as the same as the conventional central difference. Yamauchi [3] provided a formula with non-uniform discretization using the generalized Douglas scheme to increase the accuracy to second-order regardless the position of interface. Chiou *et al.* derived an improved three-point fourth-order accurate FD formula by the Taylor series expansion and matching the interface conditions for a step-index profile [4] .

The communication industry has been changed dramatically since the introduction of the Internet and broad-band access networks in last decade. As the video communication such as video telephone and video on demand (VOD) becomes popular,

fiber-to-the-home (FTTH) is proposed as a new business model which can meet the increasing demand of bandwidth. However, it is crucial for network providers to upgrade their current network without increasing revenue due to competitive market. Therefore, a key component in reducing the cost in FTTH is the optical triplexer transceiver. An FTTH network consists of an optical line termination (OLT) in central office and optical network units (ONU) in subscribers' premises. At each side of ONU, the triplexer is used to demuliplex two downstream signals to an analog receiver and a digital receiver and couple the upstream signal to the same fiber at the same time. Similarly, at the side of OLT, the triplexer combines two signal channels for downstream transmission when receiving an upstream signal from the ONUs. The commonly used commercial triplexer for FTTH passive optical network (PON) is built on assembling discrete optical components, where the wavelength demultiplexer is based on thin film filter technology [5] . This approach is very effective at producing triplexer filters with high performance, but it requires labor-intensive assemblies that reduce the industrial throughout and increase the whole cost.

Planar lightwave circuit (PLC) overcomes the shortcomings of the traditional triplexer that assembles discrete optical components; In addition, it saves more space on the chip and it is more suitable for auto-assembly and mass production.

1.2 Motivation

Improved fourth-order finite-difference method gains our interests because this method can reach fourth-order accuracy in modal analysis of step-index profile waveguide as

well as its simple algebraic form; The formulation can be easily applied to both mode solvers and propagation algorithms without significant changes. This fourth-order method uses less computation time to reach the same accuracy as the conventional first-order finite-difference method does, which is also an important reason. Since this fourth-order method doesn't increase the number of grid points, still three points, therefore no extra memory used to store the matrix.

Several new designs of triplexer have been reported based on PLC. Planar waveguide wavelength demultiplexer was investigated by Li [6] . This design uses slab waveguide to confine the beam along the vertical direction and de/multiplex three designated waves based on waveguide diffraction grating. Planar waveguide is particularly good for potential monolithic integration of optical and optoelectronic elements. But, the performance of this structure is hard to meet the bandwidth specification of ITU-T G.983 [7] . Arrayed waveguide grating (AWG) multiplexer [8] is the most widely used device used in coarse wavelength-division multiplexing (CWDM) and dense wavelength-division multiplexing (DWDM) systems. Lang proposed a triplexer filter design by using AWG [9] ; however, it has the same problem to meet the bandwidth specification of ITU-T G.983. The triplexer proposed by Shen [10] uses Bragg grating and coupler to de/multiplex three waves and shows the similar bandwidth problem. In addition, difficulties have been experienced while changing up-stream channel to 1310nm as specified in ITU-T G.983. Chen proposed a structure of using cascaded asymmetric Mach-Zehnder interferometers to yield the different bandwidth for different channels. [11] The most recently reported design by Xu [12] uses monolithically

integrated multi-mode interference (MMI) device as CWDM and uses AWG as DWDM. The simulation shows that this scheme fully meets different bandwidths for different channels specified in ITU-T G.983. Our design of triplexer filter based on silicon wire waveguide will follow Xu's idea.

1.3 Organization of Thesis

The derivation, discretization and validation of fourth-order finite-difference method are presented in Chapter 2. The application of fourth-order finite-difference method in modal analysis of thin film waveguide and optical fiber are provided in Chapter 3 and 4. Chapter 5 and 6 contain descriptions, modeling and simulation of triplexer design. The experiment setup of testing fabricated triplexer filter is contained in Chapter 7 and 8. Chapter 9 is the conclusion of thesis work

Chapter 2

Comparison between First-order FD and Fourth-order FD

In this chapter, we will derive finite-difference formulas for both first-order and fourth-order and compare the simulation results in modal analysis of dielectric optical waveguide to show that fourth-order finite-difference method is significant better than first-order finite-difference method in both computation accuracy and computation time.

2.1 Derivation of First-Order FD Discretization

2.1.1 TE Mode

Assume $E_x = 0, E_z = 0$ and $H_y = 0$ and from Maxwell's Equations we can get

$$-i\beta H_x - \left(\frac{\partial H_z}{\partial x}\right) = i\omega\varepsilon_0\mu_0 n^2 E_y \qquad [2.1]$$

$$-i\beta H_x - \left(\frac{\partial H_z}{\partial x}\right) = i\omega\varepsilon_0\mu_0 n^2 E_y \qquad [2.2]$$

$$i\beta E_y = -i\omega\mu_0 H_x \qquad [2.3]$$

$$\frac{\partial E_y}{\partial x} = -i\omega\mu_0 H_z \qquad [2.4]$$

from above equations, E_y and H_x can be expressed as

$$\frac{\partial^2 E_y}{\partial x^2}+\left(n^2k^2-\beta^2\right)E_y=0 \qquad [2.5]$$

$$\frac{\partial^2 H_x}{\partial x^2}+\left(n^2k^2-\beta^2\right)H_x=0 \qquad [2.6]$$

based on equations[2.5], [2.6]and method to every refractive index on both sides, the discretization can be expressed as

$$\frac{E_y(m+1)-2E_y(m)+E_y(m-1)}{(\Delta x)^2}+\left(n(m)^2k^2-\beta^2\right)E_y(m)=0 \qquad [2.7]$$

$$\frac{H_x(m+1)-2H_x(m)+H_x(m-1)}{(\Delta x)^2}+\left(n(m)^2k^2-\beta^2\right)H_x(m)=0 \qquad [2.8]$$

2.1.2 TM mode

Assume $E_y=0, H_x=0$ and $H_z=0$ and from Maxwell's Equations we can get

$$i\beta H_y=i\omega\varepsilon_0 n^2 E_x \qquad [2.9]$$

$$\frac{\partial H_y}{\partial x}=i\omega\varepsilon_0 n^2 E_z \qquad [2.10]$$

$$i\beta E_x+\frac{\partial E_z}{\partial x}=i\omega\mu_0 H_y \qquad [2.11]$$

from above equations, we can get equations for H_y and E_x

$$n^2\frac{\partial}{\partial x}\left(\frac{1}{n^2}\frac{\partial H_y}{\partial x}\right)+\left(n^2k^2-\beta^2\right)H_y=0 \qquad [2.12]$$

$$\frac{\partial}{\partial x}\left(\frac{1}{n^2}\frac{\partial}{\partial x}\left(n^2E_x\right)\right)+\left(n^2k^2-\beta^2\right)E_x=0 \qquad [2.13]$$

based on above equations[2.12], [2.13] and method to every refractive index on both sides, the discretization can be expressed as

$$\frac{T^E_{m+1}E_x(m+1)-\left(2-R^E_{m+1}-R^E_{m-1}\right)E_x(m)+T^E_{m-1}E_x(m-1)}{(\Delta x)^2} + \left(n(m)^2k^2-\beta^2\right)E_x(m)=0 \qquad [2.14]$$

where $T^E_{m\pm1}=\dfrac{2n^2(m\pm1)}{n^2(m\pm1)+n^2(m)}$ and $R^E_{m\pm1}=T^E_{m\pm1}-1$

$$\frac{T^H_{m+1}H_y(m+1)-\left(T^H_{m+1}-T^H_{m-1}\right)H_y(m)+T^H_{m-1}H_y(m-1)}{(\Delta x)^2} + \left(n(m)^2k^2-\beta^2\right)H_y(m)=0 \qquad [2.15]$$

where $T^H_{m\pm1}=\dfrac{2n^2(m\pm1)}{n^2(m\pm1)+n^2(m)}$

2.2 Derivation of Fourth-order FD Discretization

In order to increase the accuracy to fourth order, we have to use Taylor Expansion and boundary condition to discretize instead to discretize directly from the formulations. Therefore we cannot show explicit discretization in fourth-order situation.

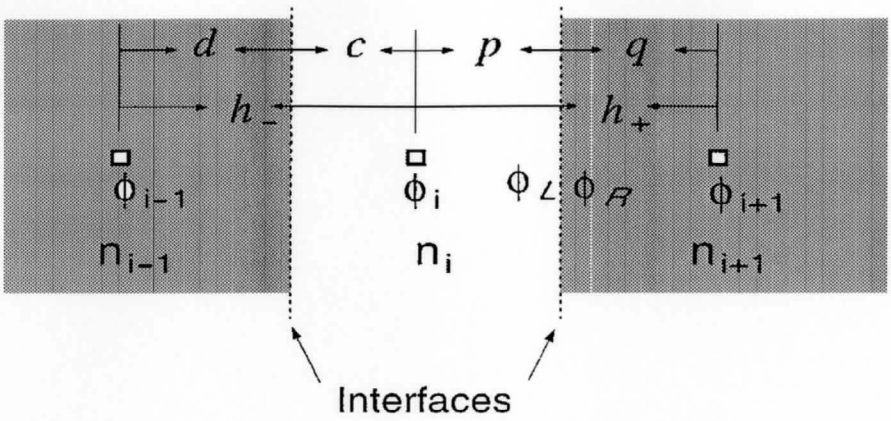

Figure 1: Sketch of interfaces between sampled points

We can consider magnetic field first. Using Taylor Expansion ϕ_L is expressed as

$$\phi_L = \phi_i + \frac{p}{1!}\frac{\partial \phi_i}{\partial x} + \frac{p^2}{2!}\frac{\partial^2 \phi_i}{\partial x^2} + \frac{p^3}{3!}\frac{\partial^3 \phi_i}{\partial x^3} + \ldots + \frac{p^j}{j!}\frac{\partial^j \phi_i}{\partial x^j} = \sum_{j=0}^{\infty} \frac{p^j}{j!}\frac{\partial^j \phi_i}{\partial x^j} \qquad [2.16]$$

so we can find a relation between ϕ_L and ϕ_i

$$p^m \frac{\partial^m \phi_L}{\partial x^m} = \sum_{j=0}^{s-m-1} \frac{p^{m+j}}{j!}\frac{\partial^{m+j} \phi_i}{\partial x^{m+j}} + O\left(h^s\right) \qquad [2.17]$$

the equation[2.17] can be expressed in matrix form

$$\bar{\phi}_L = \bar{\bar{M}}_{Li} \cdot \bar{\phi}_i + O\left(h^s\right) \qquad [2.18]$$

similarly, the matrix form of ϕ_R can be expressed as

$$\bar{\phi}_{i+1} = \bar{\bar{M}}_{+R} \cdot \phi_R + O\left(h^s\right) \qquad [2.19]$$

The interface conditions are required to match left grid point and right grid point at the interface. From Maxwell's equations, the following interface conditions can be obtained

$$\phi_R = \phi_L \qquad [2.20]$$

$$\phi_R' = \theta\phi_L' \text{ where } \theta = \begin{Bmatrix} 1, & \text{TE case} \\ n_{i+1}^2/n_i^2, & \text{TM case} \end{Bmatrix} \quad [2.21]$$

$$\phi_R'' = \phi_L'' + \eta\phi_L \quad [2.22]$$

$$\phi_R^{(3)} = \theta\phi_L^{(3)} + \theta\eta\phi_L' \quad [2.23]$$

$$\phi_R^{(4)} = \phi_L^{(4)} + 2\eta\phi_L'' + \eta^2\phi_L \quad [2.24]$$

$$\phi_R^{(5)} = \theta\left(\phi_L^{(5)} + 2\eta\phi_L'' + \eta^2\phi_L'\right) \quad [2.25]$$

or denoted as

$$\bar{\phi}_R = \bar{\bar{M}}_{RL} \cdot \bar{\phi}_L \quad [2.26]$$

higher order derivatives of ϕ_L and ϕ_R can be obtained by using Helmholtz equation. Derivation details can be found in Appendix A. From equation[2.18],[2.19] and[2.26], we can get

$$\bar{\phi}_{i+1} = \bar{\bar{M}}_+ \cdot \phi_i + O\left(h^s\right) \quad [2.27]$$

where

$$\bar{\bar{M}}_+ = \bar{\bar{M}}_{+R} \cdot \bar{\bar{M}}_{RL} \cdot \bar{\bar{M}}_{Li} \quad [2.28]$$

$\phi_{i\pm1}$ can be expressed in terms of ϕ_i can its derivatives as

$$\phi_{i-1} = e_0\phi_i + e_1\phi_i' + e_2\phi_i'' + e_3\phi_i^{(3)} + e_4\phi_i^{(4)} + e_5\phi_i^{(5)} + O\left(h^6\right) \quad [2.29]$$

$$\phi_{i+1} = f_0\phi_i + f_1\phi_i' + f_2\phi_i'' + f_3\phi_i^{(3)} + f_4\phi_i^{(4)} + f_5\phi_i^{(5)} + O\left(h^6\right) \quad [2.30]$$

where coefficients are given in appendix A. ϕ_i' and ϕ_i'' terms can be solved as

$$\phi_i' \approx \frac{f_2\phi_{i-1} + (f_0e_2 - e_0f_2)\phi_i - e_2\phi_{i+1}}{e_1f_2 - e_2f_1} = s_-\phi_{i-1} + s_0\phi_i + s_+\phi_{i+1} \equiv D_x\phi_i \qquad [2.31]$$

$$\phi_i'' \approx \frac{f_1\phi_{i-1} + (f_0e_1 - e_0f_1)\phi_i - e_1\phi_{i+1}}{e_2f_1 - e_1f_2} = t_-\phi_{i-1} + t_0\phi_i + t_+\phi_{i+1} \equiv D_x^2\phi_i \qquad [2.32]$$

combine equation [2.31]and [2.32] to eliminate ϕ_i', we can get

$$\phi_i'' \approx \frac{D_x^2\phi_i}{1 + g_1D_x + g_2D_x^2} \qquad [2.33]$$

where $g_1 = \frac{f_1e_3 - e_1f_3}{e_2f_1 - e_1f_2}$ □ $g_2 = \frac{f_1e_4 - e_1f_4}{e_2f_1 - e_1f_2}$ □ $g_3 = \frac{f_1e_5 - e_1f_5}{e_2f_1 - e_1f_2}$

the fourth-order FD will end up with

$$\frac{D_x^2\phi_i}{1 + g_1D_x + g_2D_x^2} + k_0^2n^2\phi_i = \beta^2\phi_i \qquad [2.34]$$

or

$$\begin{aligned} &D_x^2\phi_i + k_0^2n^2\left(1 + g_1D_x + g_2D_x^2\right)\phi_i \\ &= \beta^2\left(1 + g_1D_x + g_2D_x^2\right)\phi_i \end{aligned} \qquad [2.35]$$

2.3 Numerical Boundary Condition

There are several well-known numerical boundary conditions available to use, which are zero boundary condition, transparent boundary condition (TBC) and perfectly matched layer (PML) boundary condition. In order to simplify the implementation and achieve more accurate results, no complex numbers, zero boundary condition is used in both first-order and fourth-order FD simulations since we are only interested in guided modes. Yet

making the computation window big enough is very necessary to avoid reflection at the zero boundary condition.

PML boundary condition is firstly developed by J.P Berenger and required if leaky modes or radiation modes need to be calculated [14] . The parameters of the PML are determined by the reflection at the interface between the cladding and PML smaller than a give value [15] . The reflection is in the form of

$$R(0) = e^{-\frac{2}{3}\sqrt{\frac{\mu_0}{\varepsilon_0}} n_p^{-1} \alpha_{\max} \delta} \qquad [2.36]$$

where n_p is a constant refractive index of the PML medium and can be chosen to be equal to that of the cladding, δ is the thickness of PML and $\alpha_{\max}$ is the maximal conductivity of PML medium.

TBC is firstly proposed by Hardley [16] and can also be used to calculate leaky modes and radiation modes. Many researchers use TBC based on personal preference.

2.4 Solution Schemes

Solving FD method actually is equivalent to solving a large scale eigenvalue problem. There are many numerical methods to solve eigenvalue problem, yet Shifted Inverse Power Method (SIPM) and Implicit Re-Started Arnoldi Iteration are the two most wildly used methods. SIPM is a clear and easy-to-understand numerical method to solve eigenvalue problem, but SIPM can only calculate one eigenvalue every run. Instead,

Arnoldi can perform multiple eigenvalue calculation and is contained in ARPACK, a numerical software package written in Fortran 77, developed by group of researchers at Rice University [17] . Matlab includes Arnoldi as a default build-in module to solve large scale eigenvalue problem, which is a main drive to us to use Arnoldi as eigenvalue solver.

2.5 Assessment and Comparison

2.5.1 Weakly Guided Dielectric Waveguide

The investigated structure is a weakly guided symmetric dielectric slab waveguide with relative permittivity $\varepsilon_{cover} = 11.044$ in the cladding and $\varepsilon_{core} = 11.088$ in the core. The core width is $d_{core} = 2\mu$, incident light wavelength is $\lambda = 1.55\mu$ and computation window is 102μ with zero boundary condition.

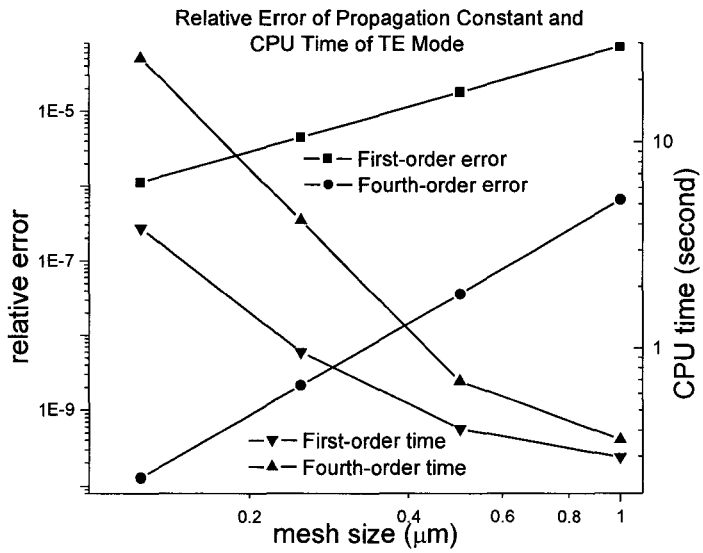

Figure 2: Relative error of propagation constant and CPU time of TE mode in weakly guiding waveguide with respect to mesh size

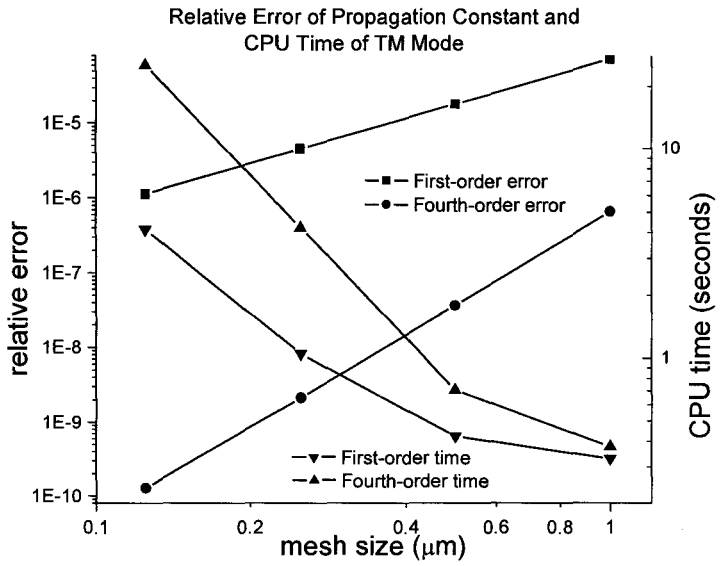

Figure 3: Relative error of propagation constant and CPU time of TM mode in weakly guiding waveguide with respect to mesh size

Figure 2 and Figure 3 show the relative error of propagation constant and CPU time with respect to mesh size. The relative error of propagation constant is defined as

$$error_{\beta} = \frac{|\beta_{cal} - \beta_{exact}|}{\beta_{exact}} \qquad [2.37]$$

the exact value of propagation constant can be obtained by analytical solution presented in [18] .

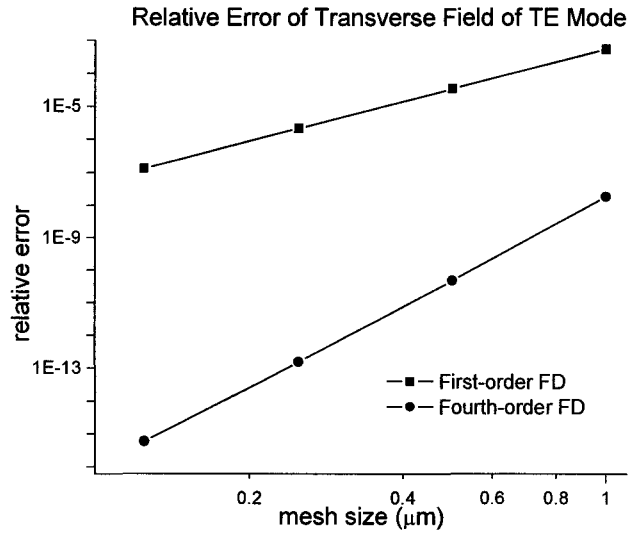

Figure 4: Relative error of transverse field of TE mode in weakly guiding waveguide with respect to mesh size

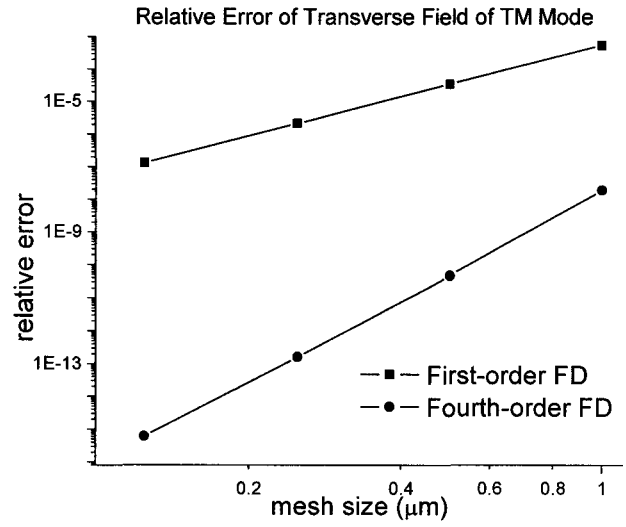

Figure 5: Relative error of transverse field of TM mode in weakly guiding waveguide with respect to mesh size

Figure 4 and Figure 5 show the relative error of transverse field with respect to mesh size. The relative error of transverse field is defined as

$$error_{field} = \frac{\sum_{i=1}^{n} (field_{cal} - field_{exact})^2}{field_{exact}^2} \qquad [2.38]$$

the exact value of field at a specific grid point can also be calculated by using analytical solutions [18] .

2.5.2 Strongly Guided Dielectric Waveguide

The investigated structure is a strongly guided symmetric dielectric slab waveguide with refractive index $n_{cladding} = 1$ in the cladding and $n_{core} = 3$ in the core. The core width is $d_{core} = 1\mu$, incident light wavelength is $\lambda = 1.55\mu$ and computation window is 102μ with zero boundary condition.

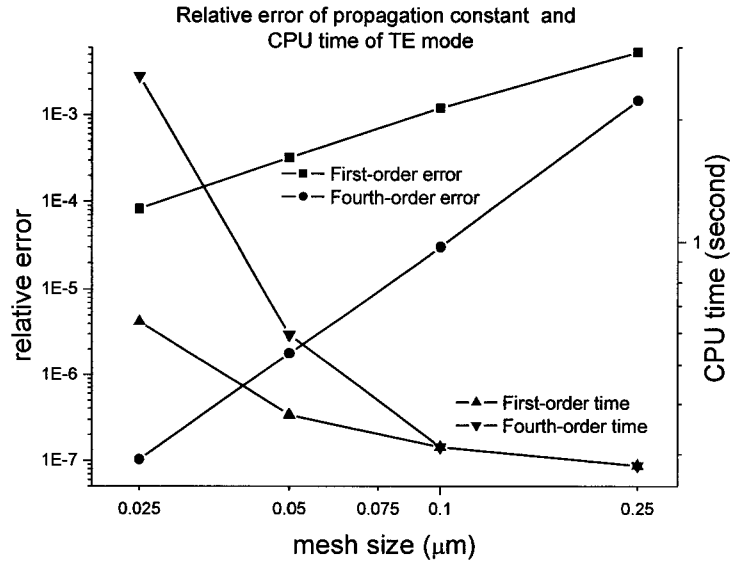

Figure 6: Relative error of propagation constant and CPU time of TE mode in strongly guiding waveguide with respect to mesh size

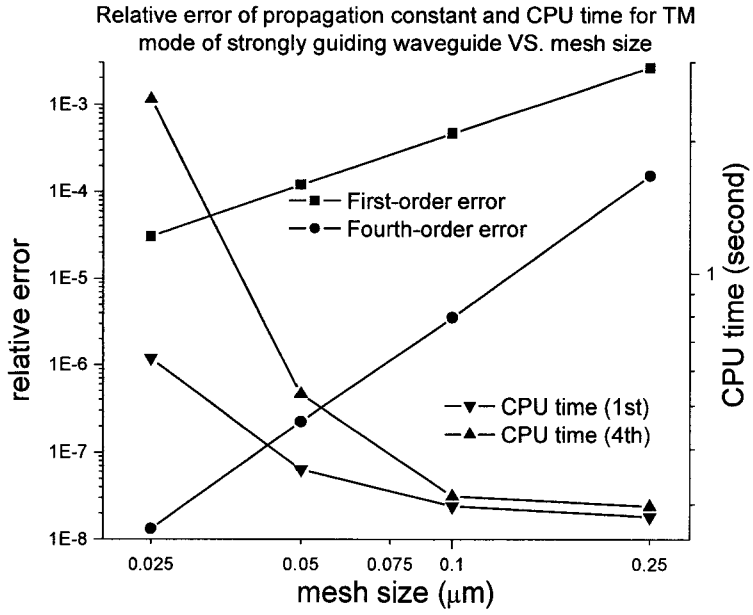

Figure 7: Relative error of propagation constant and CPU time of TM mode in strongly guiding waveguide with respect to mesh size

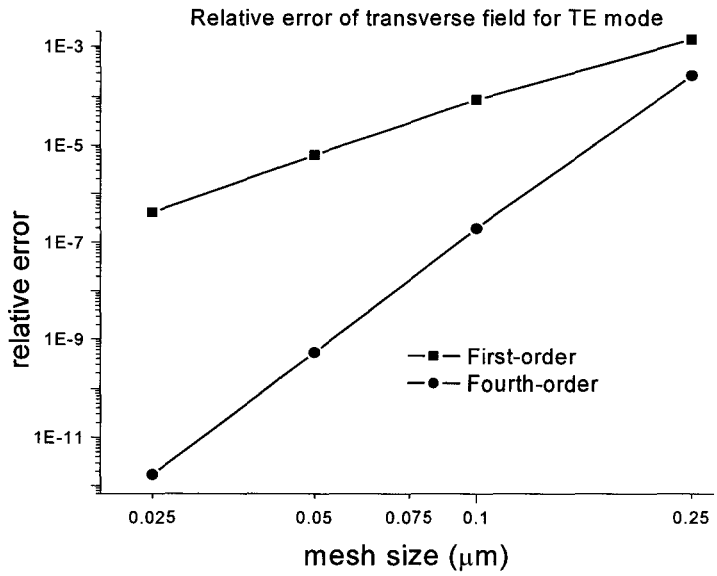

Figure 8: Relative error of transverse field of TE mode in weakly guiding waveguide with respect to mesh size

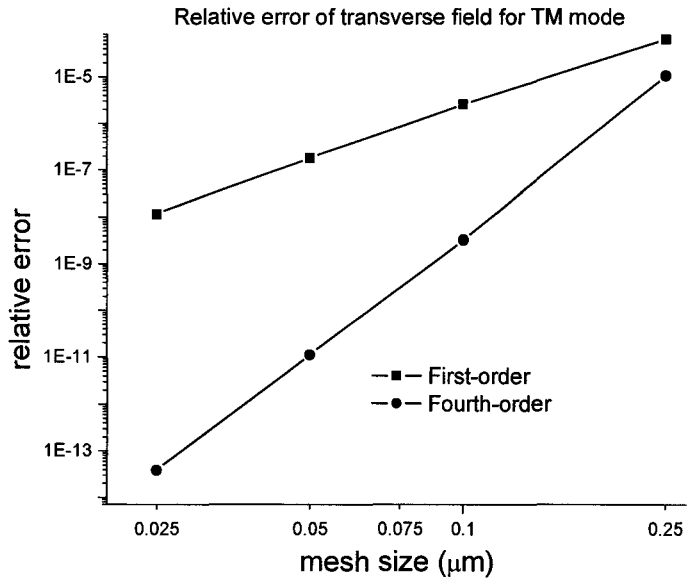

Figure 9: Relative error of transverse field of TM mode in weakly guiding waveguide with respect to mesh size

2.6 Summary

The above graphs show relative error of propagation constant, relative error of transverse field and CPU time of computation versus mesh size of both TE and TM mode in symmetric dielectric slab waveguide. It is observed that fourth-order FD is significantly better than first-order FD, the relative errors calculated by both fourth-order FD and first-order FD are linearly proportional to mesh size in log scale and the slope of fourth-order error line is bigger than the slope of first-order error line. These facts are in excellent agreement with theoretical predications. Because relative error of fourth-order FD

$\propto h^4$ and the relative error of first-order FD $\propto h$, therefore $\log(error) \propto 4\log(h)$ and $\log(error) \propto \log(h)$ for fourth-order FD and first-order FD respectively. Although fourth-order FD is more accurate than first-order FD, the computation time of fourth-order FD is longer than first-order FD for the same number of grid points used due to the more complex algorithm. But it is noticeable that fourth-order FD uses less number of grid points and less computation time than first-order FD does if the same level of accuracy is considered. Therefore we conclude that fourth-order FD is not only more accurate but also more economic in computation time than first-order FD.

Chapter 3

Application in Metal Slab Waveguide

It is a well-know property of metal materials that a transverse magnetic (TM), surface plasmon plariton (SPP), wave can be guided along their boundary with another dielectric medium [19] [20] . The size of optical waveguide using SPP can be significantly reduced compared to the conventional waveguide limited by diffraction owing to the localization of SPP along surface between metal and dielectric. The optical integrated circuit using SPP is considered as one of promising candidates for nano-scale optical circuit. In this chapter we show the superiority of using fourth-order FD to calculate guided SPP in metal slab waveguide which has huge complex refractive index contrast at interface.

3.1 Dielectric-Metal-Dielectric (DMD) Waveguide

The Dielectric-Metal-Dielectric Waveguide supports two guided SPP modes which are symmetric mode and anti-symmetric mode with respect to field distributions. Symmetric means transverse field does not exhibit to zero inside metal film, instead, anti-symmetric means transverse field exhibits to zero inside the film [21] .

Consider a waveguide with $\varepsilon_{cover} = 4$, $\varepsilon_{sub} = 4$, $\varepsilon_{core} = -19 - 0.53i$ and core width $d_{core} = 50nm$. The incident wavelength is $\lambda = 0.633\mu$ from He-Ne laser. Computation window is 8μ and zero boundary condition is used.

3.1.1 Anti-symmetric Mode

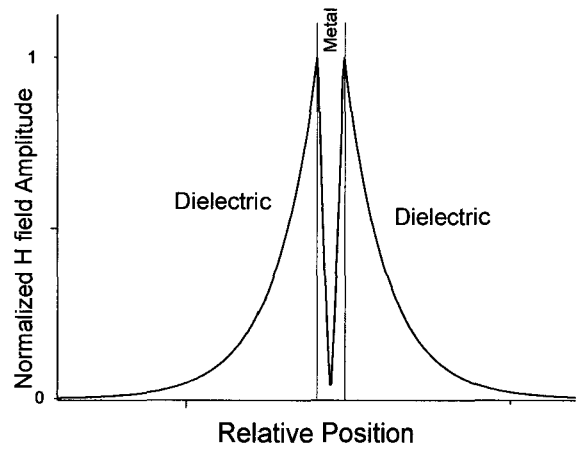

Figure 10: Modal profile of anti-symmetric mode

Figure 10 is the modal profile of anti-symmetric mode in DMD symmetric waveguide. This figure shows clearly that this mode is guided along the metal-dielectric interface and the transverse field exhibits to zero inside the thin metal film. The following three figures show the comparison between fourth-order FD and first-order FD in calculation of anti-symmetric mode.

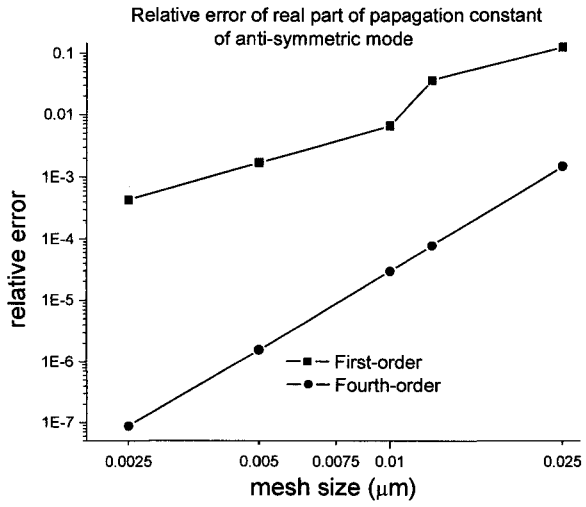

Figure 11: Relative error of real part of propagation constant of anti-symmetric mode in DMD waveguide with respect to mesh size

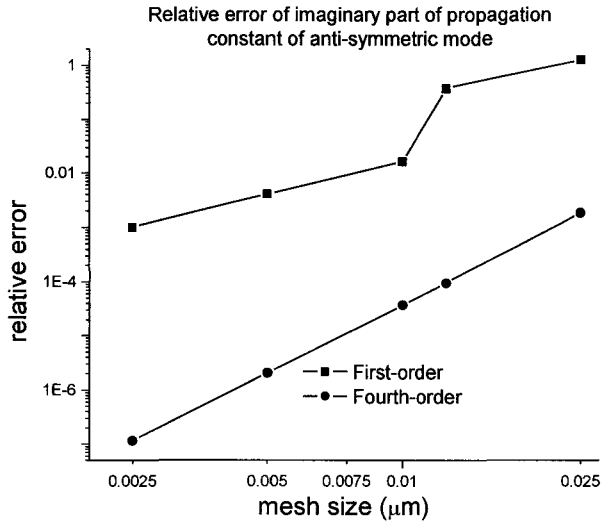

Figure 12: Relative error of imaginary part of propagation constant of anti-symmetric mode in DMD waveguide with respect to mesh size

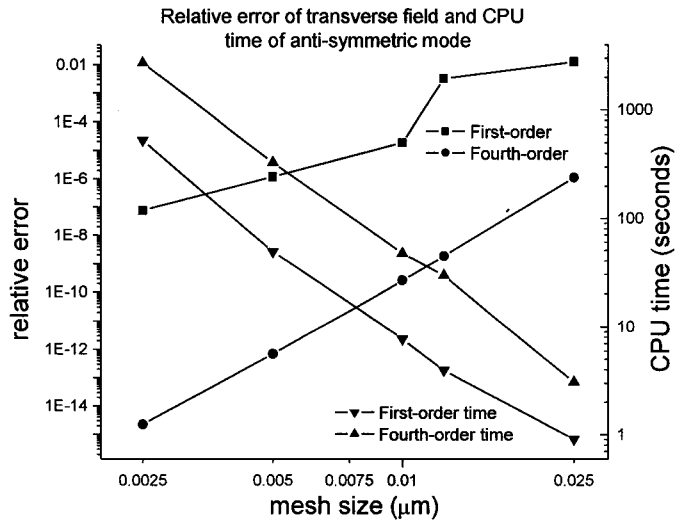

Figure 13: Relative error of transverse field and CPU time of anti-symmetric mode in DMD waveguide with respect to mesh size

The exact value of propagation constant is calculated by using reflection pole method (RPM) [22] and further refined by using Newton-Raphson [23] complex algorithm. After calculating propagation constant, we can substitute it back in transfer matrix equation to get corresponding analytical field value at every grid point. The relative error of real part and imaginary part of propagation constant are defined as

$$error_{\beta}(real) = \frac{\left|\beta_{cal}(real) - \beta_{exact}(real)\right|}{\beta_{exact}(real)} \quad [3.1]$$

$$error_{\beta}(imag) = \frac{\left|\beta_{cal}(imag) - \beta_{exact}(imag)\right|}{\beta_{exact}(imag)} \quad [3.2]$$

and the relative error of field of propagation constant is defined as

$$error_{field} = \frac{\sum_{i=1}^{n} (field_{cal} - field_{exact})^2}{field_{exact}^2} \quad [3.3]$$

3.1.2 Symmetric Mode

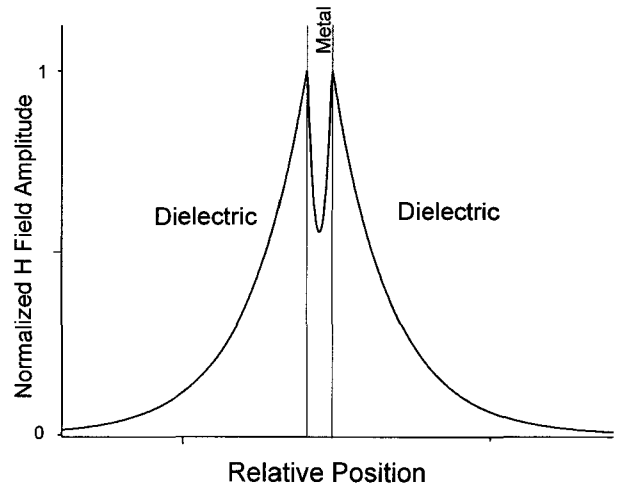

Figure 14: Modal profile of symmetric mode

Figure 14 is the modal profile of symmetric mode supported in DMD symmetric waveguide. It shows symmetric mode has two peaks along interface and the field doesn't exhibit to zero inside thin film. The following three figures show the comparison between fourth-order FD and first-order FD in calculation of symmetric mode. The exact values of propagation constant and field distributions are calculated still using RPM and Newton-Raphson algorithms.

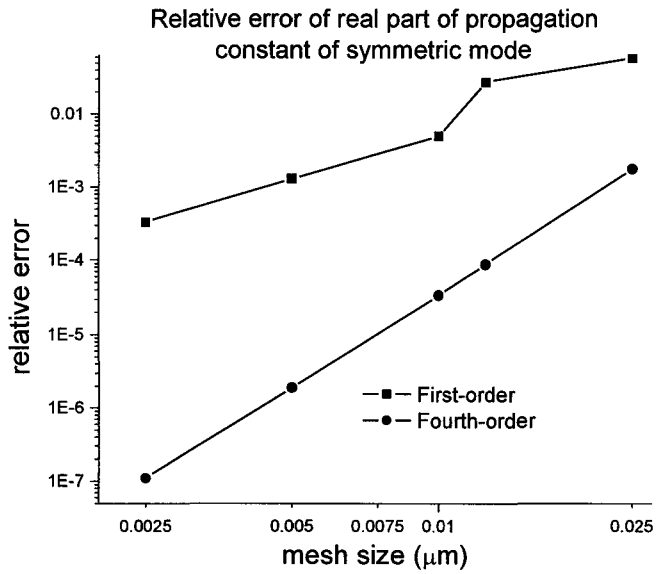

Figure 15: Relative error of real part of propagation constant of symmetric mode in DMD waveguide with respect to mesh size

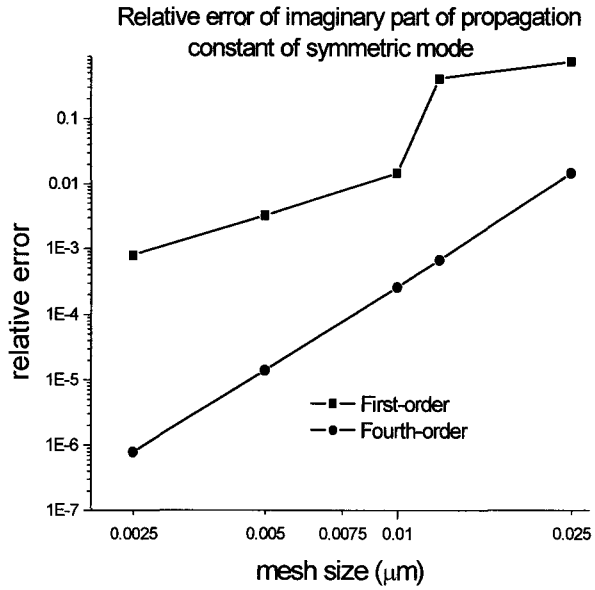

Figure 16: Relative error of imaginary part of propagation constant of symmetric mode in DMD waveguide with respect to mesh size

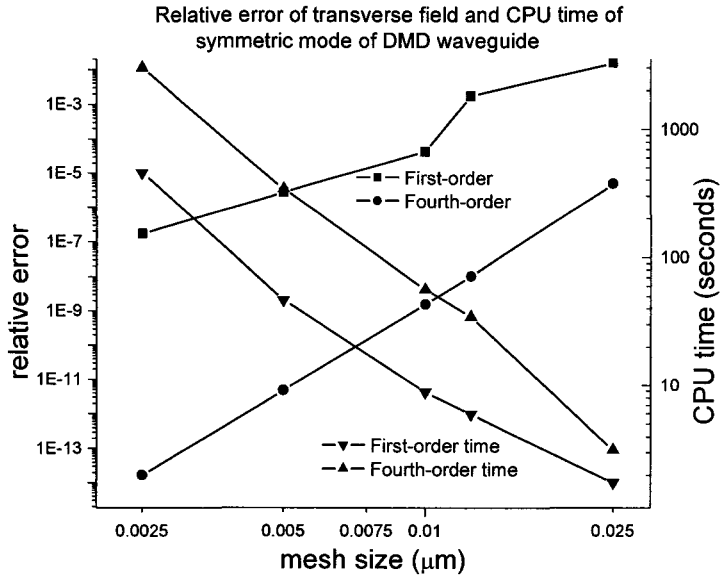

Figure 17: Relative error of transverse field and CPU time of symmetric mode in DMD waveguide with respect to mesh size

3.2 Metal-Dielectric-Metal (MDM) waveguide

This waveguide structure has permittivity of cladding $\varepsilon_{cover} = \varepsilon_{sub} = -19 - 0.53i$, permittivity of core $\varepsilon_{core} = 4$, core width $d_{core} = 50nm$ and incident light wavelength $\lambda = 0.633\mu$ .Computation window is 9μ and zero boundary condition is used. This structure supports only one guided SPP mode, different from dielectric-metal-dielectric

waveguide. The calculation of exact value of propagation constant and field in this waveguide uses reflection pole method (RPM) which is the same as the one used in DMD waveguide.

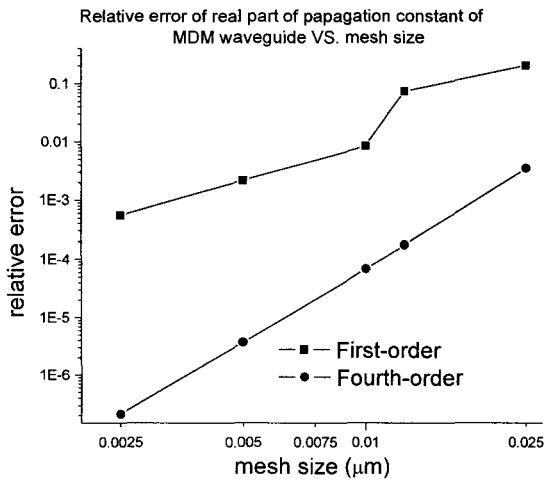

Figure 18: Relative error of real part of propagation constant of symmetric mode in MDM waveguide with respect to mesh size

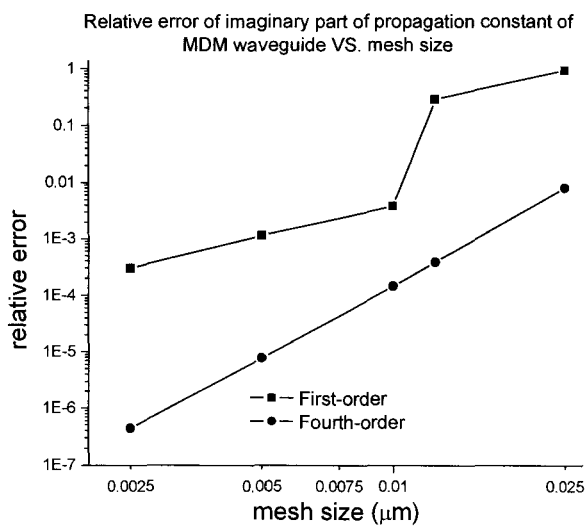

Figure 19: Relative error of imaginary part of propagation constant of symmetric mode in MDM waveguide with respect to mesh size

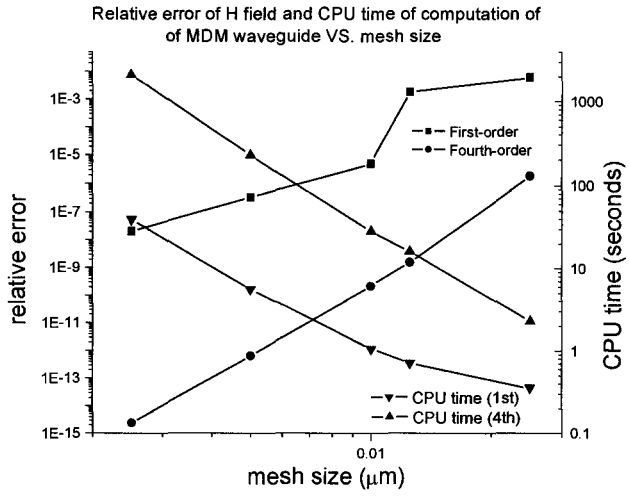

Figure 20: Relative error of transverse field and CPU time of symmetric mode in MDM waveguide with respect to mesh size

3.3 Dielectric-metal (DM) Waveguide

Conventional waveguide can support guided modes under condition that it must have more than three layers and the refractive index of core is bigger than the refractive index of cladding. However, a single interface dielectric-metal waveguide can support a guided mode at the interface owing to the fact that SPP can propagate along the surface between metal and dielectric. Let's consider a single interface waveguide with refractive index of

dielectric $n_{left} = 1.0$, refractive index of metal $n_{right} = 0.067\text{-}4.05i$ and incident light wavelength $\lambda = 1.31\mu$. Computation window is 30μ and zero boundary condition is used.

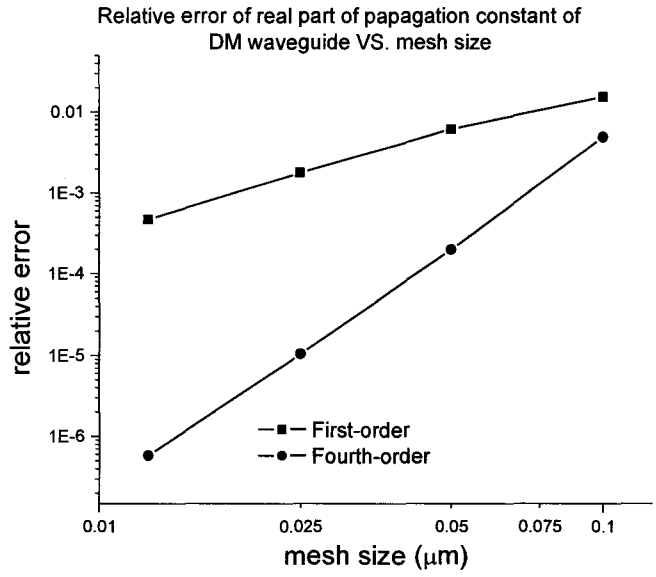

Figure 21: Relative error of real part of propagation constant of symmetric mode in MD waveguide with respect to mesh size

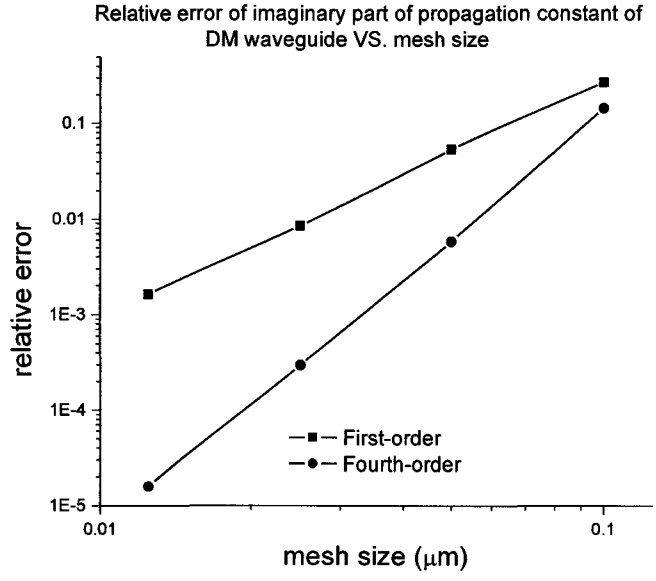

Figure 22: Relative error of imaginary part of propagation constant of symmetric mode in MD waveguide with respect to mesh size

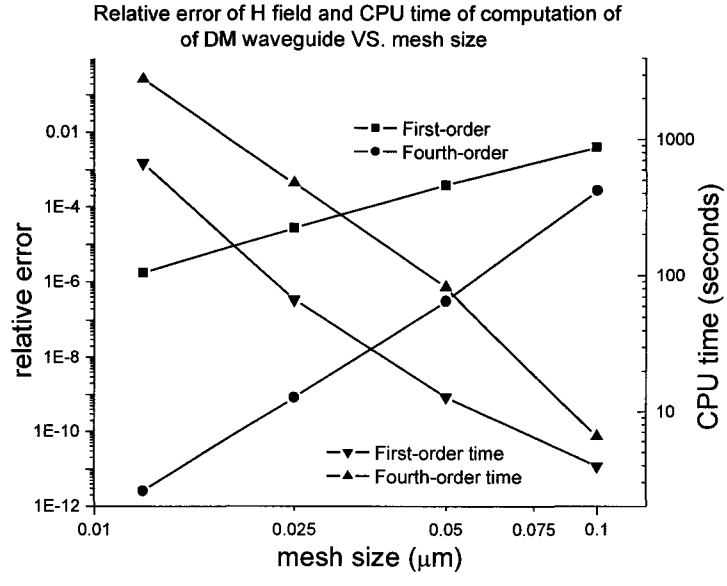

Figure 23: Relative error of transverse field and CPU time of symmetric mode in MD waveguide with respect to mesh size

3.4 Summary

This chapter compares fourth-order FD and first-order FD in modal analysis of metal slab waveguides which have huge complex refractive index contrast. The comparisons show the similar results as in dielectric slab waveguide, which fourth-order FD is not only much more accurate but also more economic in computation time than first-order FD. It is noticeable that slope of relative error calculated by first-order FD becomes smaller as the mesh size increases in metal-dielectric-metal and dielectric-metal-dielectric waveguides. This phenomenon cannot be explained properly unless the first-order FD fails if the mesh size is big. As mentioned before, the interface condition of first-order FD is averaged by refractive indexes on both sides. This method cannot work if refractive index contrast is complex and huge plus the mesh size is big. Instead, fourth-order FD matches interface conditions derived from Maxwell's equations, and this allows fourth-order FD to perform stably. Besides, we found out that first-order FD doesn't fail in single interface metal slab waveguide because mesh size and relative positions of grid points are less crucial than in two interfaces metal slab waveguide. Also, it is noticed that complexity of computation time of both first-order FD and fourth-order FD in calculation of metal waveguide is bigger than in dielectric waveguide although the same matrix eigenvalue solver is used. One possibility is that matrix computation involving complex

numbers takes more time than involving real numbers. The other possibility is that eigenvalue solver involving complex numbers is much harder to converge, which could be the major contribution of increase of computation complexity.

Chapter 4

Derivation of FD Formulas in Optical Fiber Waveguide

Optical fiber waveguide is considered as special kind of two dimensional waveguides. The cross-section of fiber waveguide is circular; therefore we can transform it from Cartesian coordinate to cylindrical coordinate, which can simplify the Helmholtz equation by using separation by variables. In this chapter, we will derive finite difference formulas for both first-order FD and fourth-order FD in optical fiber waveguide.

4.1 Derivation of Scalar Helmholtz Equation

Under weakly guiding condition, transverse fields satisfy scalar Helmholtz equation

$$\nabla^2\psi + k_0^2 n^2 \psi = 0 \qquad [4.1]$$

in cylindrical coordinate

$$\nabla^2 = \frac{\partial}{r\partial r}\left(r\frac{\partial}{\partial r}\right) + \frac{1}{r^2}\frac{\partial^2}{\partial \varphi^2} + \frac{\partial^2}{\partial z^2} \qquad [4.2]$$

scalar wave equations is thus expressed as

$$\frac{\partial}{r\partial r}\left(r\frac{\partial \psi}{\partial r}\right) + \frac{1}{r^2}\frac{\partial^2 \psi}{\partial \varphi^2} + \frac{\partial^2 \psi}{\partial z^2} + k_0^2 n^2 \psi = 0 \qquad [4.3]$$

since there is no longitudinal variation in a straight waveguide, thus $\partial/\partial z^2 = -\beta^2$. Equation [4.3] can be simplified to

$$\frac{\partial}{r\partial r}\left(r\frac{\partial \psi}{\partial r}\right)+\frac{1}{r^2}\frac{\partial^2 \psi}{\partial \varphi^2}+\left(k_0^2 n^2-\beta^2\right)\psi=0 \qquad [4.4]$$

for circular symmetric fiber, separation by variable can be used. Let's assume

$$\psi(r,\varphi)=\phi(r)\Phi(\varphi) \qquad [4.5]$$

substitute equation [4.5] into equation [4.4]

$$\frac{\partial^2 \phi(r)}{\partial r^2}\Phi(\varphi)+\frac{1}{r}\frac{\partial \phi(r)}{\partial r}\Phi(\varphi)+\frac{1}{r^2}\frac{\partial^2 \Phi(\varphi)}{\partial \varphi^2}\phi(r)+\left(k_0^2 n^2-\beta^2\right)\phi(r)\Phi(\varphi)=0 \qquad [4.6]$$

equation [4.6] can be further simplified to

$$\frac{\partial^2 \phi(r)}{\partial r^2}+\frac{1}{r}\frac{\partial \phi(r)}{\partial r}+\left(\kappa^2-\frac{\gamma^2}{r^2}\right)\phi(r)=0 \qquad [4.7]$$

if we use $\kappa^2=k_0^2 n^2-\beta^2$ and $\frac{\partial^2 \Phi(\varphi)}{\partial \varphi^2}=-\gamma^2\Phi(\varphi)$

since $\Phi(\varphi)=\Phi(\varphi+2\pi)$, it can be expressed as

$$\Phi(\varphi)=\begin{cases}\cos(\mathrm{m}\varphi)\\ \sin(\mathrm{m}\varphi)\end{cases} \quad or \quad \Phi(\varphi)=\exp(\mathrm{jm}\varphi)\ \gamma=\mathrm{m},\quad \mathrm{m}=0,1,2,\cdots \qquad [4.8]$$

substitute equation [4.8] into equation[4.7], the simplest version of scalar two dimensional Helmholtz equations in optical fiber can express as

$$\frac{\partial^2 \phi(r)}{\partial r^2}+\frac{1}{r}\frac{\partial \phi(r)}{\partial r}+\left(k_0^2 n^2-\beta^2-\frac{\mathrm{m}^2}{r^2}\right)\phi(r)=0 \qquad [4.9]$$

4.2 Derivation of FD Discretizations

4.2.1 First-order FD Discretization

By central differencing we can explicitly discretize Helmholtz equation in fiber. The second order differential operator can be expressed as

$$\left(\frac{\partial^2\phi}{\partial r^2}\right)_p = \frac{2}{(\Delta r_i + \Delta r_o)}\frac{1}{\Delta r_o}\phi_{p+1} - \frac{2}{\Delta r_i \Delta r_o}\phi_p + \frac{2}{(\Delta r_i + \Delta r_o)}\frac{1}{\Delta r_i}\phi_{p-1} \qquad [4.10]$$

and first order difference operator can be expressed as

$$\left(\frac{1}{r}\frac{\partial\phi}{\partial r}\right)_p = \frac{1}{r_p}\frac{1}{(\Delta r_i + \Delta r_o)}\phi_{p+1} - \frac{1}{r_p}\frac{1}{(\Delta r_i + \Delta r_o)}\phi_{p-1} \qquad [4.11]$$

substitute equation [4.10] and equation [4.11] into equation[4.9], we can get first-order central differencing FD formula in circular optical fiber

$$\begin{aligned}&\frac{1}{(\Delta r_i + \Delta r_o)}\left(\frac{2}{\Delta r_o} + \frac{1}{r_p}\right)\phi_{p+1} + \left(k_0^2 n^2 - \frac{m^2}{r^2} - \frac{2}{\Delta r_i \Delta r_o}\right)\phi_p \\ &+ \frac{1}{(\Delta r_i + \Delta r_o)}\left(\frac{2}{\Delta r_i} - \frac{1}{r_p}\right)\phi_{p-1} = \beta^2\phi_p\end{aligned} \qquad [4.12]$$

4.2.2 Fourth-order FD Discretization

If we want to increase the accuracy to fourth-order, then we have to use Taylor Expansion and boundary condition to discretize instead to discretize directly from the formulations. Therefore we cannot show explicit discretization in fourth-order situation. The method to get fourth-order FD formula in optical fiber is similar to the method in slab waveguide except we have to re-derive boundary conditions and expression for

coefficients e and f because Helmholtz equations change in optical fiber. Derivation of interface conditions and expressions of coefficients e and f can be found in appendix B

Besides we have to get an explicit expression ϕ_i' from equation [2.31]and[2.32] as

$$\phi_i' \approx \frac{D_x \phi_i}{1 + h_2 D_x^2} \qquad [4.13]$$

Where $h_2 = \frac{f_2 e_3 - e_2 f_3}{e_1 f_2 - e_2 f_1}$.

substitute equation [4.13] and [2.33] into equation[4.9], we can have FD formula for fourth-order accuracy in optical fiber as

$$\frac{D_x^2 \phi_i}{1 + g_1 D_x + g_2 D_x^2} + \frac{1}{r_i} \frac{D_x \phi_i}{1 + h_2 D_x^2} + \left(k_0^2 n^2 - \frac{\mathrm{m}^2}{r_i^2} \right) \phi_i = \beta^2 \phi_i \qquad [4.14]$$

4.3 Summary

The initiative of using fourth-order FD is to still use three points to increase accuracy and save computation time. In slab waveguide, fourth-order FD can be used because the Helmholtz equation doesn't have first order derivative terms. Instead, in optical fiber, the Helmholtz equation can be discretized into equation[4.14]. If operator $1 + g_1 D_x + g_2 D_x^2$ and $1 + h_2 D_x^2$ are multiplied on both sides of the equation, the it will look like

$$\begin{aligned}&\left(1+h_2D_x^2\right)D_x^2\phi_i+\frac{1}{r_i}\left(1+g_1D_x+g_2D_x^2\right)D_x\phi_i\\&+\left(1+h_2D_x^2\right)\left(1+g_1D_x+g_2D_x^2\right)\left(k_0^2n^2-\frac{\mathrm{m}^2}{r_i^2}\right)\phi\\&=\left(1+h_2D_x^2\right)\left(1+g_1D_x+g_2D_x^2\right)\beta^2\phi_i\end{aligned} \qquad [4.15]$$

The corresponding matrix form of equation [4.15]is not a tri-diagonal matrix, which means we implicitly used more than three points after discretization although we only used three points at the beginning. This shows that it is impossible to reach fourth-order accuracy by using Taylor expansion and matching interface conditions in optical waveguide although we can simplify this two dimensional structure to one dimension using separation of variables.

Chapter 5

Description of Filter Design

The design of triplexer is based on divide-and-conquer strategy. According to ITU G.983 standard that the bandwidths are 100nm, 20nm and 10nm for laser at 1310nm, DPIN at 1490nm and APIN at 1555nm respectively. Firstly, we use a 2x2 multi-mode interference device (MMI) [25] to select wavelength at 1310nm, then we use a 1x2 arrayed waveguide grating (AWG) as a DWDM for wavelength at 1490 and 1555. Figure 24 shows the schematic design. The reason we use MMI and AWG is that design scheme is simple and clear, and bandwidths at different wavelengths can be easily satisfied. In addition to achieving different bandwidths, this design can maximally lower the cross-talk between down-stream signals and up-stream signals. The up-stream laser signal received by laser is the most detrimental for performance of system. ITU-T G.984.2 [25] specifies ONU has maximum mean launched power of 7dBm, minimum sensitivity of -28dBm and minimum extinction ratio of 10dB. Therefore, the isolation between 1490nm and 1310nm should be bigger than 45dBm. Due to multiple filtering by both MMI and AWG, this cross-talk is extremely weak. We use silicon wire as base waveguide because minimum bending radius is only several micro meters and the length of AWG can be made very small. Another important reason is cost can be very low for high volume production.

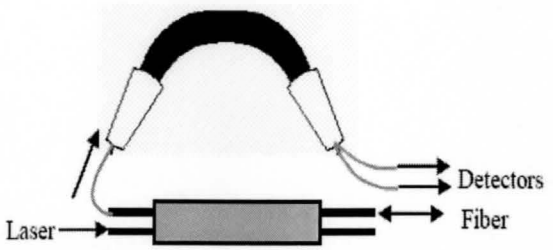

Figure 24: Schematic design of triplexer filter

Chapter 6

Modeling and Simulation Results

6.1 Single mode condition

Before we simulate MMI and AWG, we have to calculate the single mode condition and the minimum bending radius of the silicon wire waveguide. The single mode condition requires that the first high order mode is leaky and its effective index is less than the refractive index of cladding. In our design, thickness of waveguide is 340nm and it cannot be changed due to fabrication specification given by the foundry. We need to change the width of waveguide and make sure this waveguide has only one guided mode at this thickness and width. Figure 25 shows the leaky loss and effective index of the first high order mode by using APSS [26] . From this figure, we can tell that the width has to be smaller or equal to $0.5\mu m$ to satisfy the single mode condition. In order to make the design safe, we take the width of channel at $0.35\mu m$. Figure 26 shows the cross-sectional structure of the waveguide we will in our design.

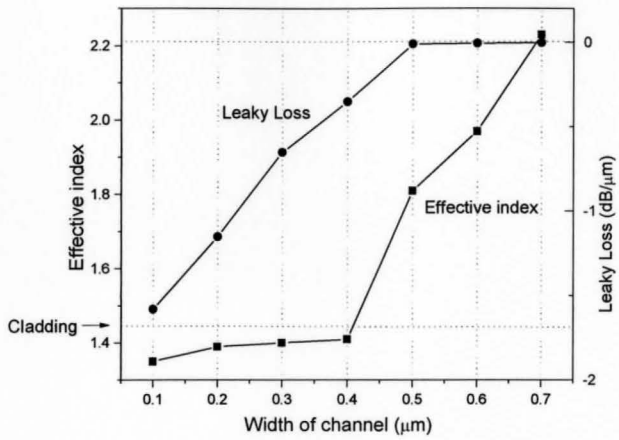

Figure 25: Effective index and leaky loss of the first high order mode

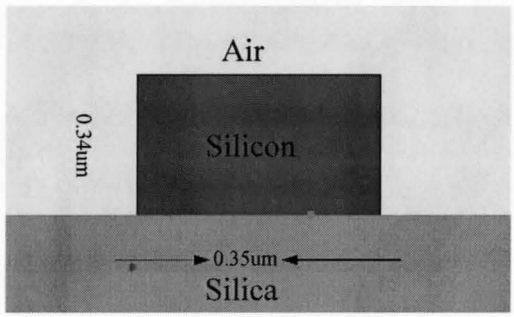

Figure 26: Cross-sectional structure of silicon wire waveguide

6.2 Minimum Bending Radius

Besides the single mode condition, we also have to consider the minimum bending radius of waveguide. Waveguide bending is inevitable in planar lightwave circuit, and the bending loss is due to radiation at bend. The device cannot function well if bending loss is too high. Since we use AWG in our design, the minimum bending radius of the waveguide affects performance and size of AWG significantly. The simulation results of

minimum bending radius of the waveguide is done by using APSS and showed in Figure 27

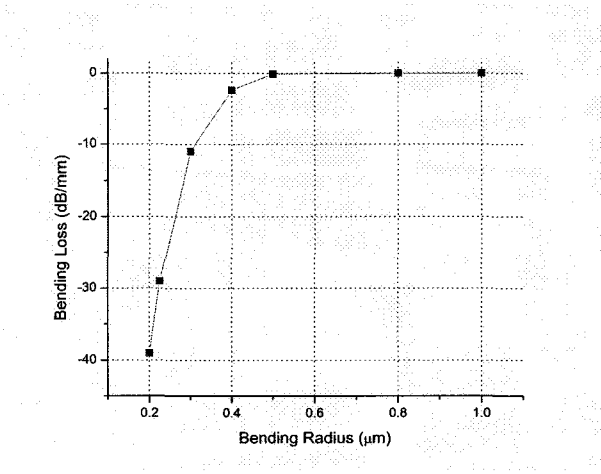

Figure 27: Bending loss of fundamental mode

Figure 27 shows that bending radius of silicon wire, strongly guiding waveguide, can be really small, less than $1\mu m$. Therefore the bending radius of AWG has to be bigger than the minimum bending radius of the waveguide. Actually, the bending radius of AWG is $10\mu m$ in our design, which is much bigger than minimum bending radius.

6.3 MMI as CWDM

Figure 28 shows the conventional MMI in which input and output ports are not tapered. But simulation result in Figure 29 shows this conventional MMI cannot give desired spectrum response in terms of flatness. We have to optimize the design of input and output ports to make the output spectrum response flat.

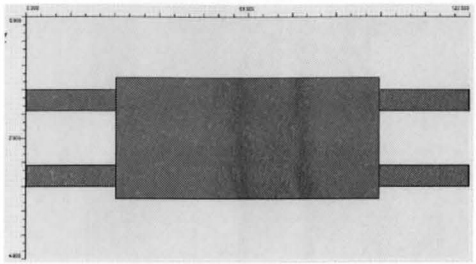

Figure 28: Layout of conventional MMI

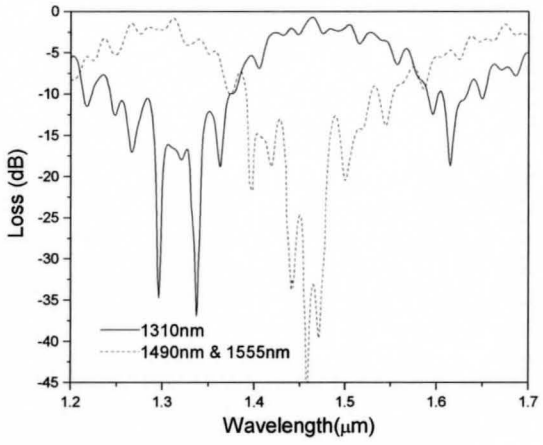

Figure 29: Simulation result of conventional MMI without optimization

After testing on different taper shapes, we finally end up with the design in Figure 30. The width of MMI is $2\mu m$, the length of coupler is $73\mu m$, and the length of port is $125\mu m$. The spectrum response of MMI is in Figure 31. The simulated spectrum response shows two peaks at 1310nm and 1522nm. The insertion loss at central wavelength at 1310nm and the 100nm span around central wavelength are -0.15dB and -0.75dB. Therefore, the passing band is very wide and flat.

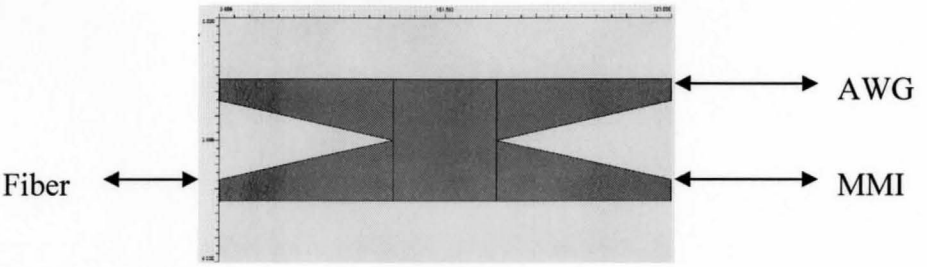

Figure 30: Schematic layout of MMI

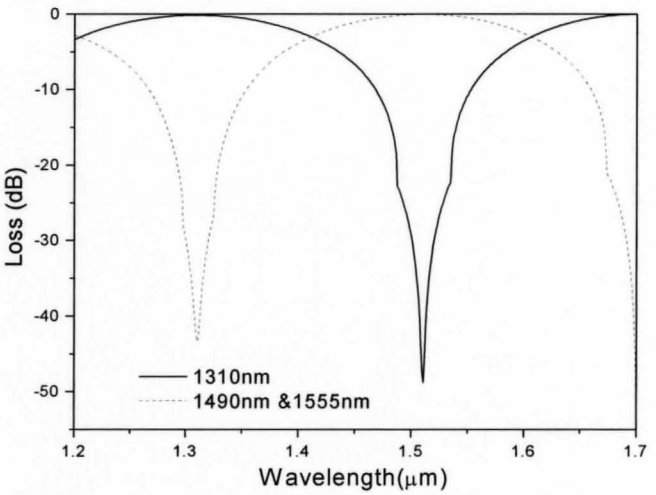

Figure 31: Simulation result of MMI

The above design is the one after optimization on input port. If we use conventional MMI without optimization, the spectrum response would not give us desired bandwidth in terms of spectral flatness.

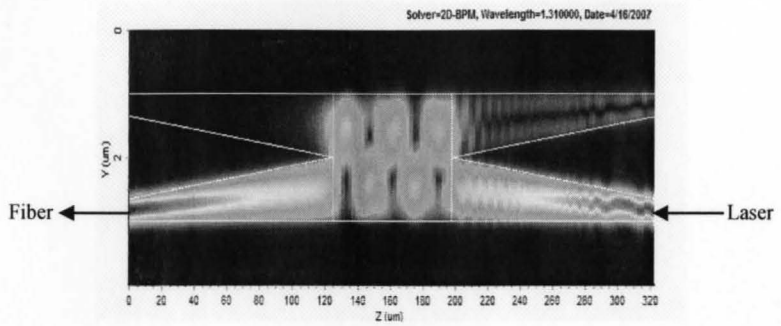

Figure 32: Field pattern of the optimized MMI at 1310nm

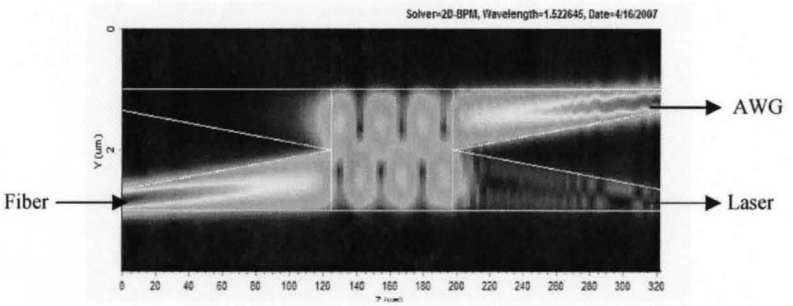

Figure 33: Field pattern of the optimized MMI at 1522nm

By examining field pattern of laser input at 1310nm and field pattern of fiber input at 1522nm, as shown in Figure 32 and Figure 33, we found some light with very low power, less than -40dB, goes into another port. This will not lead to any cross-talk for the end-to-end triplexer filter performance because the light is carried mainly by high order leaky modes and these modes will leak out before reaching the output port due to single mode condition at the output port.

6.4 AWG as DWDM

The two down-stream signals have relative big bandwidths and large spacing between them. Besides, MMI filters as a CWDM before AWG. Therefore, the free spectral range (FSR) has to be very big, larger than 200nm. We know that for AWG

$$\Delta f_{FSR} = \frac{c}{\tilde{N}_g \Delta L} \qquad [6.1]$$

where $\tilde{N}_g$ is the group index of the waveguide mode defined as

$$\tilde{N}_g = N_g + f\frac{dN_g}{df} \qquad [6.2]$$

where N_g is the effective index of the waveguide mode. The Above equations can be found in [8] .

After calculation we found out that path difference between adjacent array wavguides has to be extremely small, less than $5\mu m$, in order to achieve big FSR and desired bandwidth in our case.

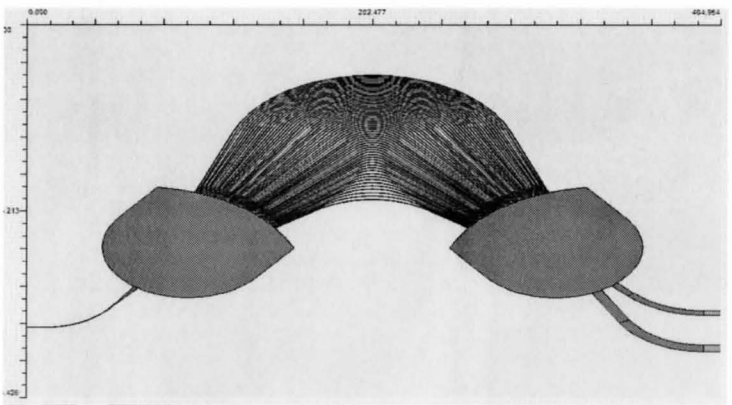

Figure 34: Layout of the AWG

After tried my numbers of combinations, we finally found the following layout shown in Figure 34. In this final design, the Rowland arc couplers are tilted 53^0, separated by 275 μm and total 60 array waveguides can be fit in between. The path difference between adjacent array waveguides is 3.54 μm. We also optimized on input port and array waveguides to achieve the minimum insertion loss. However, it is unnecessary to optimize the output ports of AWG because they are directly connected to detectors. Figure 35 shows simulation result.

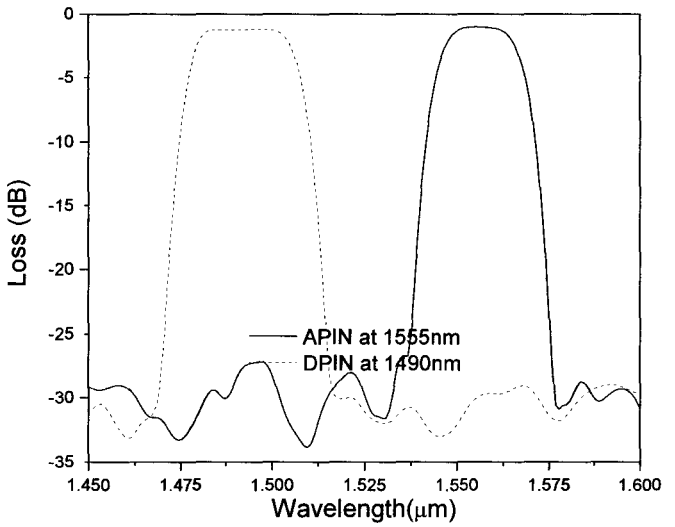

Figure 35: Simulation result of AWG

6.5 Integrated Circuit

By integrating optimized 2x2 MMI and 1x2 AWG, we could construct an integrated circuit shown in Figure 36.

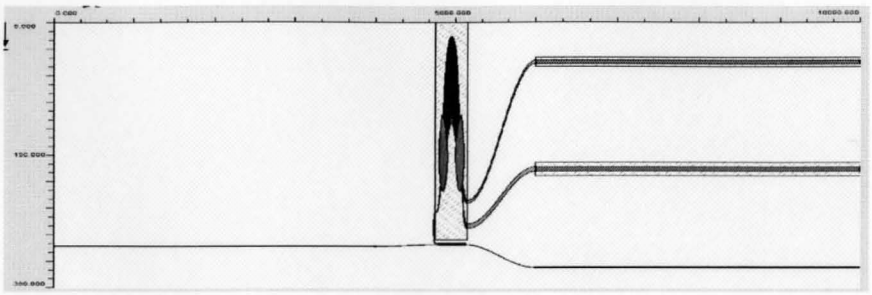

Figure 36: Layout of integrated circuit

We can see from Figure 36 that AWG and MMI are both very small, less than $500\mu m \times 500\mu m$. But we make the length of integrated circuit at $1cm$ to make sure AWG and MMI won't be damaged during post-fabrication process, such as cleaving and polishing. The integrated circuit can be made this small all due to extremely small minimum bending radius of silicon wire waveguide. The simulation result of end-to-end spectral response of triplexer filter performed by APSS is showed in Figure 37 The desired spectrum and bandwidths at 1310nm, 1490nm and 1555nm are achieved. But we also found the power to detector at 1310nm is around -13dB, which can be solved by putting Anti-reflective Coating on cross-sectional surface of the chip.

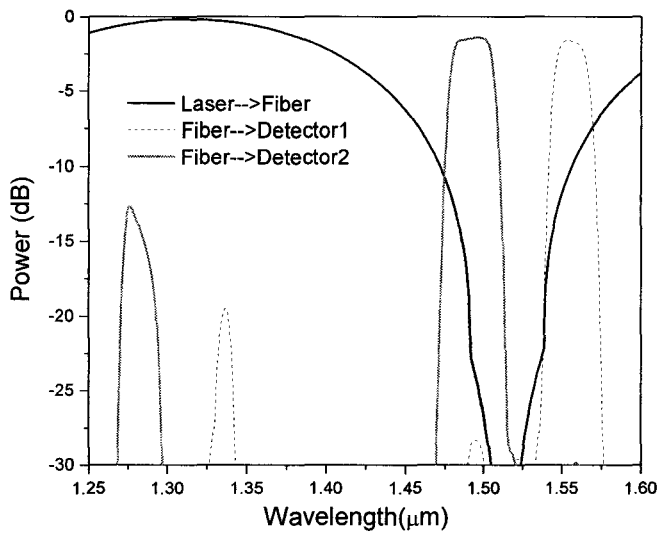

Figure 37: Simulation of integrated circuit

In order to clarify Figure 37 , we summarized important datum of simulation result of the whole triplexer filter in Table 1.

Table 1: Summary of simulation result of triplexer filter

Central Wavelength λ_0 (nm)	Wavelength Span $\Delta\lambda$ (nm)	Loss at $\lambda_0 - \Delta\lambda$ (dB)	Loss at λ_0 (dB)	Loss at $\lambda_0 + \Delta\lambda$ (dB)
1310	100	-0.83	-0.17	-0.72
1490	20	-2.39	-1.49	-1.57
1555	10	-1.86	-1.63	-1.88

6.6 Fabrication Considerations

The foundry provides E-Beam lithography for fabrication silicon wire based devices. The maximal patch size is $500\mu m \times 500\mu m$ and stitch error is 10nm. In addition, the fabrication tolerance of E-Beam lithography is 10nm. Therefore, we have to take these uncertainties into considerations during our design. But we don't need to worry about over-etching and under-etching thanks to the working mechanic of E-Beam Lithography.

The width of MMI is very touchy, so we have to design several MMIs with the same parameters but different width. The with of array waveguides, path difference between adjacent array waveguides and positions of output ports on star couplers of AWG are all relatively sensitive, which forces us to design more AWGs with different parameters in mentioned prospective. So the number of combinations is more than 20, and we finally decided to fabricate only 20 circuits after considering relative importance among these combinations and fabrication cost.

As mentioned before, we make the length of the integrated circuit at 1cm to make sure AWG and MMI won't be damaged after cleaving and polishing. The ports distance is $150\mu m$, bigger than diameter of multi-mode fiber, to guarantee that fiber can be fit in during test. Figure 38 shows mask layout drew by AutoCAD.

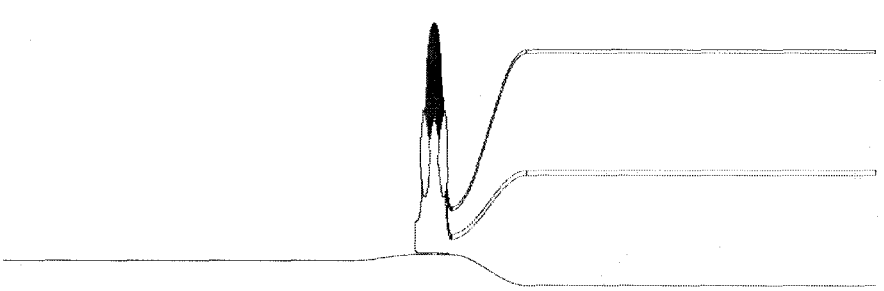

Figure 38: Mask layout of integrated circuit

Chapter 7

Actual Device and Its Pictures

7.1 SEM Pictures

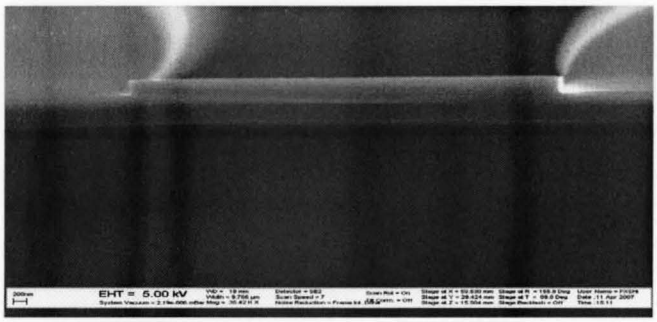

Figure 39: SEM picture of cross-section

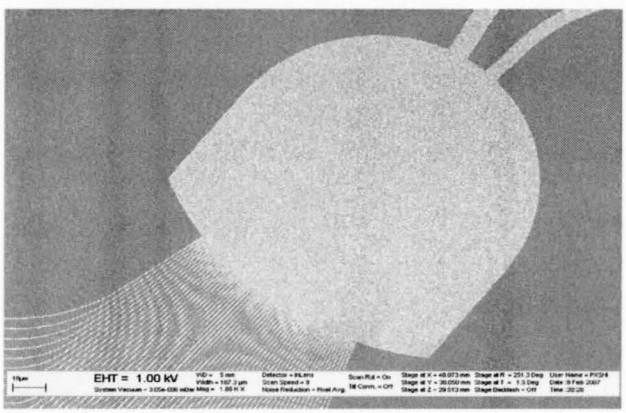

Figure 40: SEM picture of star coupler of AWG

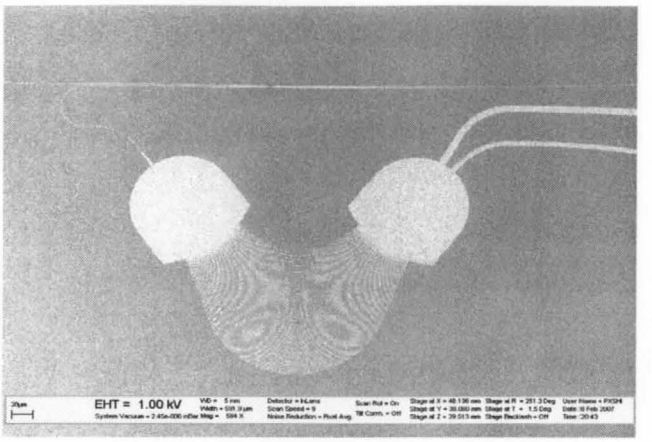

Figure 41: SEM picture of top view of triplexer filter

7.2 Microscopic Pictures

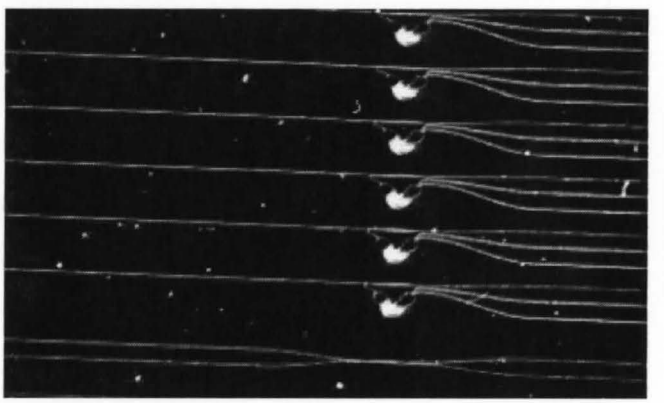

Figure 42: Microscopic picture of top view of triplexer filter

Chapter 8

Experimental Set-up and Testing

8.1 Experimental Set-up

The experimental set-up can be seen in Figure 43

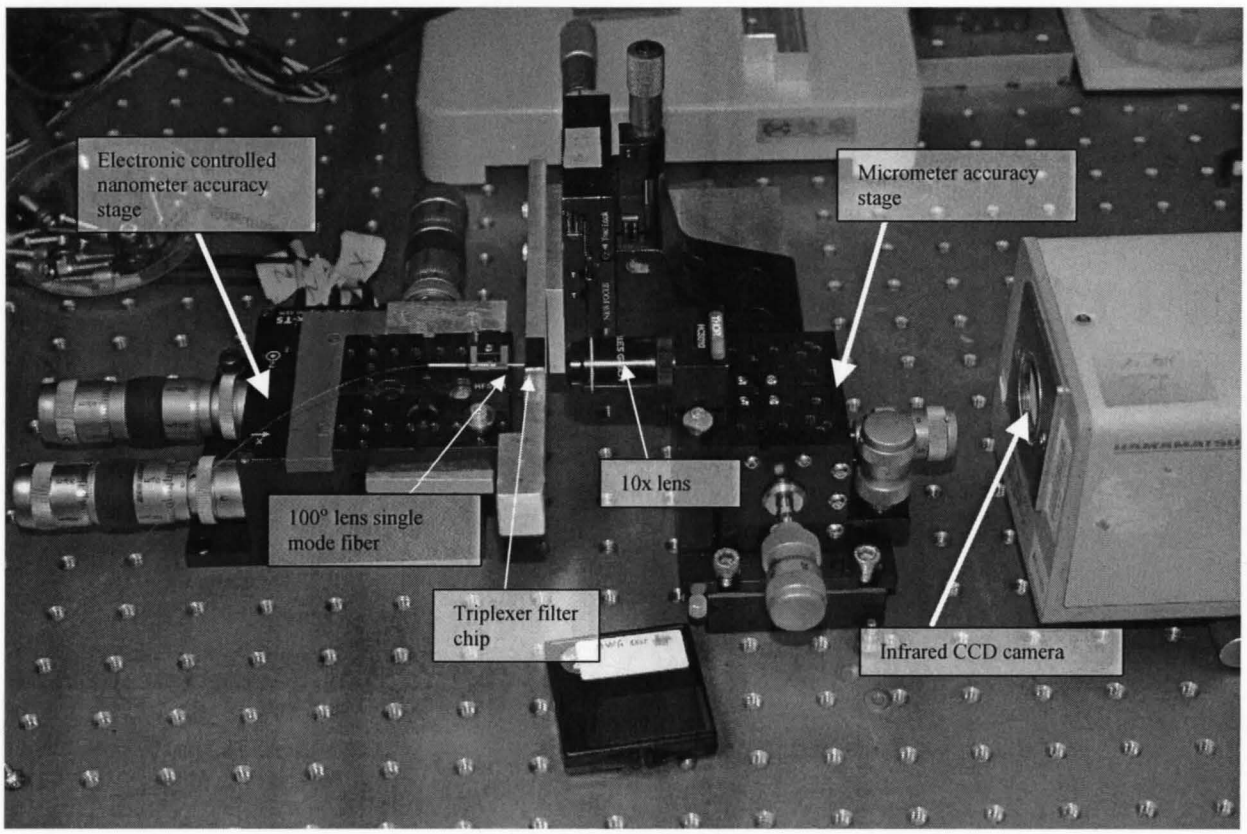

Figure 43: Experimental set-up for testing triplexer filter

8.2 Test Procedures

We first connect single mode fiber with He-Ne laser at lasing wavelength $0.6327\mu m$, visible red light. The red light can help us on aligning lens fiber, input port of triplexer filter and CCD camera due to very small area of cross section of filter. After finishing adjust the alignment, we can change input wavelength from $0.6327\mu m$ to $1310nm$. Now, we are able to see a field pattern through infrared CCD camera on the other side. This step can let us know if the light is coupled into waveguide or not. If we see light coming out of waveguide, we can put multi-mode fiber connected with optical power meter of which sensitivity can go as high as -70dBm.

Chapter 9

Conclusions

We showed that improved three-point fourth-order finite difference method is significant better than conventional first-order finite difference method in modal analysis of optical waveguides which includes both dielectric slab waveguides and metal waveguides that support SPP. The superiority shows in both computation accuracy and computation time. But we found out that this fourth-order finite difference method is only limited to one dimensional waveguides and this method doesn't work on a optical fiber waveguide which can be reduced to one dimension using separation by variables.

We also showed modeling, simulation, and fabrication of triplexer optical filter based on silicon wire waveguide in FTTH passive optical networks. The results show that the design meets all required spectral specifications in terms of bandwidth and stream isolation. Besides it can be made in a very small scale on 3 inch or 5 inch silicon wafer. Therefore, we say this design is suitable for high volume production with low cost in telecommunication industry.

Appendix A

Helmholtz equation in slab waveguide is

$$\frac{\partial^2 \phi}{\partial x^2} + k^2 n^2 \phi = \beta^2 \phi \qquad [A.1]$$

from Maxwell's curl equation we can get

$$\phi_R = \phi_L \qquad [A.2]$$

$$\phi_R' = \theta \phi_L' \text{ where } \theta = \begin{Bmatrix} 1, & \text{TE case} \\ n_{i+1}^2 / n_i^2, & \text{TM case} \end{Bmatrix} \qquad [A.3]$$

right point – left point in equation [A.1]

$$\frac{\partial^2 \phi_R}{\partial x^2} - \frac{\partial^2 \phi_L}{\partial x^2} + k^2 n_R^2 \phi_R - k^2 n_L^2 \phi_L = 0 \qquad [A.4]$$

or denoted as

$$\phi_R'' = \phi_L'' + \eta \phi_L \qquad [A.5]$$

where $\eta = k^2 n_L^2 - k^2 n_R^2$

take derivative on both sides of equation [A.1] we can get

$$\frac{\partial^3 \phi}{\partial x^3} + k^2 n^2 \phi' = \beta^2 \phi' \qquad [A.6]$$

right point – left point in equation [A.6], we get

$$\phi_R^{(3)} - \theta\phi_L^{(3)} + k^2 n_R^2 \phi_R{}' - \theta k^2 n_L^2 \phi_L{}' = 0 \qquad [A.7]$$

which can be simplified to

$$\phi_R^{(3)} = \theta\phi_L^{(3)} + \theta\eta\phi_L' \qquad [A.8]$$

take derivative on both sides of equation [A.6]

$$\phi^{(4)} + k^2 n^2 \phi'' = \beta^2 \phi'' \qquad [A.9]$$

right point – left point of equation [A.9]

$$\phi_R^{(4)} - \phi_L^{(4)} + k^2 n_R{}^2 \phi_R{}'' - k^2 n_L{}^2 \phi_L{}'' = \beta^2 \left(\phi_R{}'' - \phi_L{}''\right) \qquad [A.10]$$

and we know $\beta^2\phi = \phi'' + k^2 n^2 \phi$, so we get

$$\phi_R^{(4)} = \phi_L^{(4)} + 2\eta\phi_L'' + \eta^2\phi_L \qquad [A.11]$$

take the derivative on both sides of equation [A.9]

$$\phi^{(5)} + k^2 n^2 \phi^{(3)} = \beta^2 \phi^{(3)} \qquad [A.12]$$

tight point – left point of equation [A.12]

$$\phi_R^{(5)} = \theta\left(\phi_L^{(5)} + 2\eta\phi_L'' + \eta^2\phi_L'\right) \qquad [A.13]$$

Coefficients of e and f are listed below

Appendix B

Helmholtz equation in optical fiber is

$$\frac{\partial^2\phi}{\partial r^2}+\frac{1}{r}\frac{\partial\phi}{\partial r}+\left(k^2n^2-\frac{m^2}{r^2}\right)\phi=\beta^2\phi \qquad [B.1]$$

and

$$\phi_L=\phi_R \qquad [B.2]$$

$$\frac{\partial\phi_L}{\partial r}=\frac{\partial\phi_R}{\partial r} \qquad [B.3]$$

right point – left point in equation [B.1]

$$\frac{\partial^2\phi_R}{\partial r^2}=\frac{\partial^2\phi_L}{\partial r^2}+\eta\phi_L \qquad [B.4]$$

take derivative on both sides of [B.1]

$$\phi^{(3)}+\frac{1}{r}\frac{\partial^2\phi}{\partial r^2}-\frac{1}{r^2}\frac{\partial\phi}{\partial r}+\left(k^2n^2-\frac{m^2}{r^2}\right)\frac{\partial\phi}{\partial r}+\frac{2m^2}{r^3}\phi=\beta^2\frac{\partial\phi}{\partial r} \qquad [B.5]$$

right point – left point in equation [B.5]

$$\phi_R^{(3)}=\phi_L^{(3)}+\eta\frac{\partial\phi_L}{\partial r}-\frac{\eta}{r}\phi_L \qquad [B.6]$$

take derivative on both sides of equation [B.5]

$$\phi^{(4)}+\frac{1}{r}\frac{\partial^3\phi}{\partial r^3}+\left(k^2n^2-\frac{m^2+2}{r^2}\right)\frac{\partial^2\phi}{\partial r^2} +\frac{4m^2+2}{r^3}\frac{\partial\phi}{\partial r}-\frac{6m^2}{r^4}\phi=\beta^2\frac{\partial^2\phi}{\partial r^2} \quad [B.7]$$

right point – left point in equation [B.7]

$$\phi_R^{(4)}-\phi_L^{(4)}+\frac{1}{r}\left(\frac{\partial^3\phi_R}{\partial r^3}-\frac{\partial^3\phi_L}{\partial r^3}\right)+\left(k^2n_R^2\frac{\partial^2\phi_R}{\partial r^2}-k^2n_L^2\frac{\partial^2\phi_L}{\partial r^2}\right) -\frac{m^2+2}{r^2}\left(\frac{\partial^2\phi_R}{\partial r^2}-\frac{\partial^2\phi_L}{\partial r^2}\right)=\beta^2(\eta\phi_L) \quad [B.8]$$

and from equation [B.1], we know $\beta^2\phi_L=\frac{\partial^2\phi_L}{\partial r^2}+\frac{1}{r}\frac{\partial\phi_L}{\partial r}+\left(k^2n_L^2-\frac{m^2}{r^2}\right)\phi_L$, Substitute it into equation [B.8]

$$\phi_R^{(4)}=\phi_L^{(4)}+2\eta\frac{\partial^2\phi_L}{\partial r^2}+\eta\left(\eta+\frac{3}{r^2}\right)\phi_L \quad [B.9]$$

take derivative on both sides of equation [B.7]

$$\phi^{(5)}+\frac{1}{r}\frac{\partial^4\phi}{\partial r^4}+\left(k^2n^2-\frac{m^2+3}{r^2}\right)\frac{\partial^3\phi}{\partial r^3}+\frac{6m^2+6}{r^3}\frac{\partial^2\phi}{\partial r^2} -\frac{18m^2+6}{r^4}\frac{\partial\phi}{\partial r}+\frac{24m^2}{r^5}\phi=\beta^2\frac{\partial^3\phi}{\partial r^3} \quad [B.10]$$

right point – left point in equation [B.10]

$$\phi_R^{(5)} - \phi_R^{(5)} + \frac{1}{r}\left(\frac{\partial^4\phi_R}{\partial r^4} - \frac{\partial^4\phi_L}{\partial r^4}\right) + \left(k^2 n_R^2 \frac{\partial^3\phi_R}{\partial r^3} - k^2 n_L^2 \frac{\partial^3\phi_L}{\partial r^3}\right) - \frac{m^2+3}{r^2}\left(\frac{\partial^3\phi_R}{\partial r^3} - \frac{\partial^3\phi_L}{\partial r^3}\right)$$
$$+ \frac{6m^2+6}{r^3}\left(\frac{\partial^2\phi_R}{\partial r^2} - \frac{\partial^2\phi_L}{\partial r^2}\right) - \frac{18m^2+6}{r^4}\left(\frac{\partial\phi_R}{\partial r} - \frac{\partial\phi_L}{\partial r}\right) \qquad [B.11]$$
$$+ \frac{24m^2}{r^5}(\phi_R - \phi_L) = \beta^2\left(\frac{\partial^3\phi_R}{\partial r^3} - \frac{\partial^3\phi_L}{\partial r^3}\right)$$

left hand side of [B.11]

$$= \phi_R^{(5)} - \phi_R^{(5)} + \frac{1}{r}\left(2\eta\frac{\partial^2\phi_L}{\partial r^2} + \eta\left(\eta + \frac{3}{r^2}\right)\phi_L\right) - \eta\frac{\partial^3\phi_L}{\partial r^3} + k^2 n_R^2\left(\eta\frac{\partial\phi_L}{\partial r} - \frac{\eta}{r}\phi_L\right)$$
$$- \frac{m^2+3}{r^2}\left(\eta\frac{\partial\phi_L}{\partial r} - \frac{\eta}{r}\phi_L\right) + \frac{6m^2+6}{r^3}\eta\phi_L$$

right hand side of [B.11]

$$= \beta^2\left(\eta\frac{\partial\phi_L}{\partial r} - \frac{\eta}{r}\phi_L\right)$$

from equation [B.1] and [B.5] we know

$$\beta^2\phi_L = \frac{\partial^2\phi_L}{\partial r^2} + \frac{1}{r}\frac{\partial\phi_L}{\partial r} + \left(k^2 n_L^2 - \frac{m^2}{r^2}\right)\phi_L$$

$$\beta^2\frac{\partial\phi_L}{\partial r} = \phi_L^{(3)} + \frac{1}{r}\frac{\partial^2\phi_L}{\partial r^2} + \left(k^2 n_L^2 - \frac{m^2+1}{r^2}\right)\frac{\partial\phi_L}{\partial r} + \frac{2m^2}{r^3}\phi_L$$

The right hand side of equation [B.11] becomes

$$\eta\left(\phi_L^{(3)} + \frac{1}{r}\frac{\partial^2\phi_L}{\partial r^2} + \left(k^2 n_L^2 - \frac{m^2+1}{r^2}\right)\frac{\partial\phi_L}{\partial r} + \frac{2m^2}{r^3}\phi - \frac{1}{r}\frac{\partial^2\phi_L}{\partial r^2} - \frac{1}{r^2}\frac{\partial\phi_L}{\partial r} - \frac{1}{r}\left(k^2 n_L^2 - \frac{m^2}{r^2}\right)\phi_L\right)$$

$$\eta\left(\phi_L^{(3)} + \left(k^2 n_L^2 - \frac{m^2+2}{r^2}\right)\frac{\partial\phi_L}{\partial r} - \frac{1}{r}\left(k^2 n_L^2 - \frac{3m^2}{r^2}\right)\phi_L\right)$$

we can derive fifth order boundary condition from both sides of equation [B.11]

$$\phi_R^{(5)} - \phi_L^{(5)} - \eta\frac{\partial^3\phi_L}{\partial r^3} + \frac{2\eta}{r}\frac{\partial^2\phi_L}{\partial r^2} + k^2 n_R^2\frac{\partial\phi_L}{\partial r} - \eta\frac{m^2+3}{r^2}\frac{\partial\phi_L}{\partial r} +$$
$$\frac{\eta}{r}\left(\left(\eta+\frac{3}{r^2}\right) - k^2 n_R^2 + \frac{12m^2+9}{r^2}\right)\phi_L = \eta\frac{\partial^3\phi_L}{\partial r^3} + \eta\left(k^2 n_L^2 - \frac{m^2+2}{r^2}\right)\frac{\partial\phi_L}{\partial r}$$
$$-\frac{\eta}{r}\left(k^2 n_L^2 - \frac{3m^2}{r^2}\right)\phi_L$$

which can be simplified to

$$\phi_R^{(5)} = \phi_L^{(5)} + 2\eta\frac{\partial^3\phi_L}{\partial r^3} - \frac{2\eta}{r}\frac{\partial^2\phi_L}{\partial r^2} + \eta\left(\eta+\frac{1}{r^2}\right)\frac{\partial\phi_L}{\partial r} - \frac{\eta}{r}\left(2\eta + \frac{4m^2+12}{r^2}\right)\phi_L \quad [B.12]$$

Coefficients of e and f are listed below

$$f_0 = 1 + \frac{\eta h^2}{8} - \frac{\eta h^3}{48r} + \frac{\eta h^4}{384}\left(\eta+\frac{3}{r^2}\right) - \frac{\eta h^5}{3840r}\left(\eta - \frac{4m^2+12}{r^2}\right) \quad [B.13]$$

$$f_1 = h + \frac{\eta h^3}{12} - \frac{\eta h^4}{96r} + \frac{\eta h^5}{768}\left(\eta+\frac{3}{r^2}\right) + \frac{\eta^2 h^5}{3840} \quad [B.14]$$

$$f_2 = \frac{h^2}{2} + \frac{\eta h^4}{32} - \frac{\eta h^5}{320r} \quad [B.15]$$

$$f_3 = \frac{h^3}{6} + \frac{\eta h^5}{120} \quad [B.16]$$

$$f_4 = \frac{h^4}{24} \quad [B.17]$$

$$f_5 = \frac{h^5}{120} \quad [B.18]$$

$$e_0 = 1 - \frac{h^2}{8}\eta - \frac{1}{48}\frac{h^3\eta}{r} + \frac{1}{384}\frac{h^4\eta\left(\eta r^2 - 3\right)}{r^2} + \frac{1}{3840}\frac{h^5\eta\left(3\eta r^2 + 12 + 4m^2\right)}{r^3} \quad [B.19]$$

$$e_1 = -h + \frac{h^3\eta}{12} + \frac{1}{48}h^3\eta + \frac{1}{96}\frac{h^4\eta}{r} - \frac{1}{768}\frac{h^5\eta\left(\eta r^2 - 3\right)}{r^2} - \frac{1}{3840}\frac{h^5\eta^2}{r^2} \quad [B.20]$$

$$e_2 = \frac{h^2}{2} - \frac{h^4\eta}{32} - \frac{1}{320}\frac{h^5\eta}{r} \quad [B.21]$$

$$e_3 = -\frac{h^3}{6} + \frac{1}{120}h^5\eta \quad [B.22]$$

$$e_4 = \frac{h^4}{24} \quad [B.23]$$

$$e_5 = -\frac{h^5}{120} \quad [B.24]$$

Bibliography

[1] M. S. Stern, "Semivectorial polarized finite difference method for optical waveguides with arbitrary index profiles," *Inst. Elect. Eng. Proc. –J.* **135**, 56-63 (1988).

[2] C. Vassallo, "Improvement of finite difference methods for step-index optical waveguides," *Inst. Elect. Proc. –J.* **139**, 137-142 (1992)

[3] J, Yamauchi, M. Sekiguchi, O. Uchiyama, J. Shibayama and H. Nakano, "Modified finite-difference formula for the analysis of semivectorial modes in step-index optical waveguides," *IEEE Photo. Technol. Lett.*, **9**, 961-963 (1997)

[4] Y. –P. Chiou, Y. –C. Chiang, H. –C. Chang, "Improved three-point formulas considering the interface conditions in the finite-difference analysis of step-index optical devices," *J. Lightwave Technol.* **18**, 243-251 (2000).

[5] M. Yanagisawa *et al.*, "Low-loss and compact TFF-embedded silica-waveguide WDM filter for video distribution services in FTTH systems," in *Proc. OFC 2004*, Los Angeles, CA, Feb. 2004, p. TuI4

[6] X. Li *et al.*, "A novel planar waveguide wavelength demultiplexer design for integrated optical triplexer transceiver," *IEEE Photon. Technol. Lett.* **17**, 1214-1216, 2005

[7] ITU-T G.983, "A broadband optical access system with increased service capability by wavelength allocation."

[8] M. K Smit and C.Van Dam, "PHASAR-based WDM-devices: Principles,

design and applications," *IEEE J. Sel. Topics Quantum Electron.*, vol. 2, no.3, pp. 136-250, 2006

[9] T. Lang *et al.*, "Cross-order arrayed waveguide grating design for triplexers in fiber access networks," *IEEE Photon. Technol. Lett.* **18**, 232-234, 2006

[10] L. P. Shen *et al.*, "Integrated grating-assisted coarse/dense WDM multiplexers," *in Optical components and devices, Proc. SPIE* **5577**, 698-706, 2004

[11] W. Chen *et al*, "Compact, low loss chip scale triplexer WDM filter," *Optical fiber communication conference, post deadline paper*, 2006

[12] C. Xu *et al.*, "Design optimization of integrated BiDi triplexer optical filter based planar lightwave circuit", *Optics Express* vol.**14**, no. 11, 2006

[13]

[14] J. P. Berenger, "A perfectly matched layer for the electromagnetic-waves" *J. Computational Physics* **114**, 185-200 (1994)

[15] W.P. Huang, C. L. Xu, W. Lui, "The perfectly matched layer (PML) boundary condition for the beam propagation method," *IEEE Photo. Technol. Lett.*, **8**, 649-651 (1996)

[16] G. R. Hardley, R. E. Smith, "Full-vector wave-guide modeling using an iterative finite-difference method with transparent boundary-conditions," *J. Lightwave Technol.* **13**, 465-469 (1995)

[17] http://www.caam.rice.edu/software/ARPACK/

[18] D. Marcuse, Theory of dielectric optical waveguides, 1974

[19] E. N. Economou, "Surface plasmons in thin films," *Phys. Rev.* **182**, 539 (1969)

[20] D. N. Mirlin, Electromagnetic Waves at surfaces and interfaces, 1982

[21] J. J. Burke, G. I. Stegeman and T. Tamir, "Surface-polariton-like waves guided by thin, lossy metal films," *Phys. Rev. B* **33**, 5186 (1986)

[22] Anemogiannis E, Glytsis EN, Gaylord TK□"Determination of guided and leaky modes in lossless and lossy planar multilayer optical waveguides: Reflection pole method and wavevector density method," *J. Lightwave Technol.* **17**, 929-941 (1999)

[23] M. Attenborough, Mathematics for electrical engineering and computing, 2003

[24] L.B. Soldano and C. M. Pennings, "Optical multimode interference devices based on self-imaging: principles and applications," *J. Lightwave Technol* **13**, 615-627 (1995)

[25] ITU-T G.984.2, "Gigabit-capable passive optical networks (GPON): Physical media dependent (PMD) layer specification."

[26] APSS, Apollo Photonics Solution Suite, Apollo Inc., Hamilton, Ontario, Canada